*minerals*

MDPI

*Article*

# Alteration and Mineralization Products of the Zannone Giant Pockmark (Zannone Hydrothermal Field, Central Tyrrhenian Sea)

**Aida Maria Conte [1], Letizia Di Bella [2], Michela Ingrassia [1], Cristina Perinelli [2,*] and Eleonora Martorelli [1]**

[1] C.N.R.—Istituto di Geologia Ambientale e Geoingegneria, Sede di Roma, c/o Dipartimento di Scienze della Terra, Sapienza Università di Roma, P.le A. Moro, 5, 00185 Roma, Italy; aidamaria.conte@cnr.it (A.M.C.); michela.ingrassia@igag.cnr.it (M.I.); eleonora.martorelli@igag.cnr.it (E.M.)

[2] Dipartimento di Scienze della Terra, Sapienza Università di Roma, P.le A. Moro, 5, 00185 Roma, Italy; letizia.dibella@uniroma1.it

* Correspondence: cristina.perinelli@uniroma1.it

Received: 28 May 2020; Accepted: 23 June 2020; Published: 27 June 2020


**Abstract:** The Zannone Giant Pockmark (ZGP) is a shallow-water (<−150 m) giant depression located on the shelf off Zannone Island (Pontine Archipelago, central Tyrrhenian Sea, Italy), hosting active hydrothermal vents. The ZGP seabed displays different fluid-venting morphologies (pockmarks, lithified pavements, mounds, and cone-shaped structures) and widespread bacterial communities. In this study, we analyzed ROV (Remote Operated Vehicle) images to gain information on seabed geology and the textural, mineralogical, and geochemical composition of authigenic crusts and gravel-sized clasts sampled close to active emissions. ROV images show authigenic dome-shaped crusts composed of native sulfur associated with barite, gypsum, amorphous silica, and secondary hydrothermal minerals (illite–montmorillonite). The gravel-sized clasts are mostly rhyolites strongly affected by hydrothermal alteration (Alteration Index > 88; depletion of some mobile elements and enrichment of some base metals), causing feldspar-destruction, silicification, formation of hydrothermal phyllosilicates, and precipitation of disseminated pyrite. More intense alteration implying the complete obliteration of the primary mineralogy or fabric is represented by quartz-pyrite samples. ZGP seabed morphology and petro-geochemical features of deposits point to the possible occurrence of a sulfide system linked to the degassing of magma similar to that feeding the Pleistocene products of Ponza Island.

**Keywords:** hydrothermal alteration geochemistry; volcanogenic massive sulfide deposits; Zannone Giant Pockmark; Pontine Archipelago

## 1. Introduction

Seafloor hydrothermal systems developed in subduction related to tectonic environments are characterized by distinctive feature, such as: (1) fluid venting zones located at relatively shallow water depth (<1600 m) and low hydrostatic pressure; (2) acidic host rock composition; and (3) a significant magmatic degassing or magmatic contribution of volatiles and metals to the hydrothermal system (e.g., Reference [1,2]). These features differ from those recognized at mid-ocean ridges where the deep water location decreases the likelihood of boiling during fluid ascent and venting [2].

Shallow water hydrothermal systems, although mainly recognized along the western Pacific and Mid-Atlantic Ridge, have been also documented in the Tyrrhenian Sea (Panarea and Palinuro volcanoes), where massive sulfide deposits and fragments have been found [3]. Research on the

hydrothermal occurrences of the Tyrrhenian Sea highlights the importance of host rock controls on the nature of seafloor hydrothermal systems and related mineral deposits [4].

As a whole, research on these systems is improving our understanding of hydrothermal alterations and elemental cycling. It can provide useful knowledge for ore-deposits formation and their style of mineralization, as well as for alteration associated with hydrothermal fluids (e.g., Reference [5,6]).

In arc and back-arc submarine environments, a broad range of hydrothermal fluid compositions can be found and magmatic volatiles can significantly influence fluid–rock reactions and promote chemical exchange between the hosting rocks, sediment and overlying water column. In addition, the contribution of magmatic fluids to hydrothermal fluid chemistry has received much attention in the context of ore-deposit formation (e.g., Reference [7–10]). It has been suggested that magmatic fluids may contain levels of magma-derived metals that may represent the source of metals in hydrothermal fluids responsible for ore formation [11,12].

The study area (Figure 1) belongs to the Zannone hydrothermal field, a shallow-water hydrothermal system recently discovered in the submarine sector of Zannone Island. The Zannone hydrothermal field is characterized by giant depressions developed on a NE–SW morpho-structural high, off the Italian peninsula (central Tyrrhenian Sea), where three main volcanic islands (i.e., Palmarola, Ponza, and Zannone) formed during the Plio-Pleistocene (4.5–1.0 Ma [13]) in the back-arc setting of the Tyrrhenian Sea. Volcanic products basically consist of Pliocene rhyolites and Pleistocene trachytes and alkaline to peralkaline rhyolites [13,14]. Moreover, at Zannone Island, Triassic basement and meso-Cenozoic sedimentary units locally crop out below volcanic units.

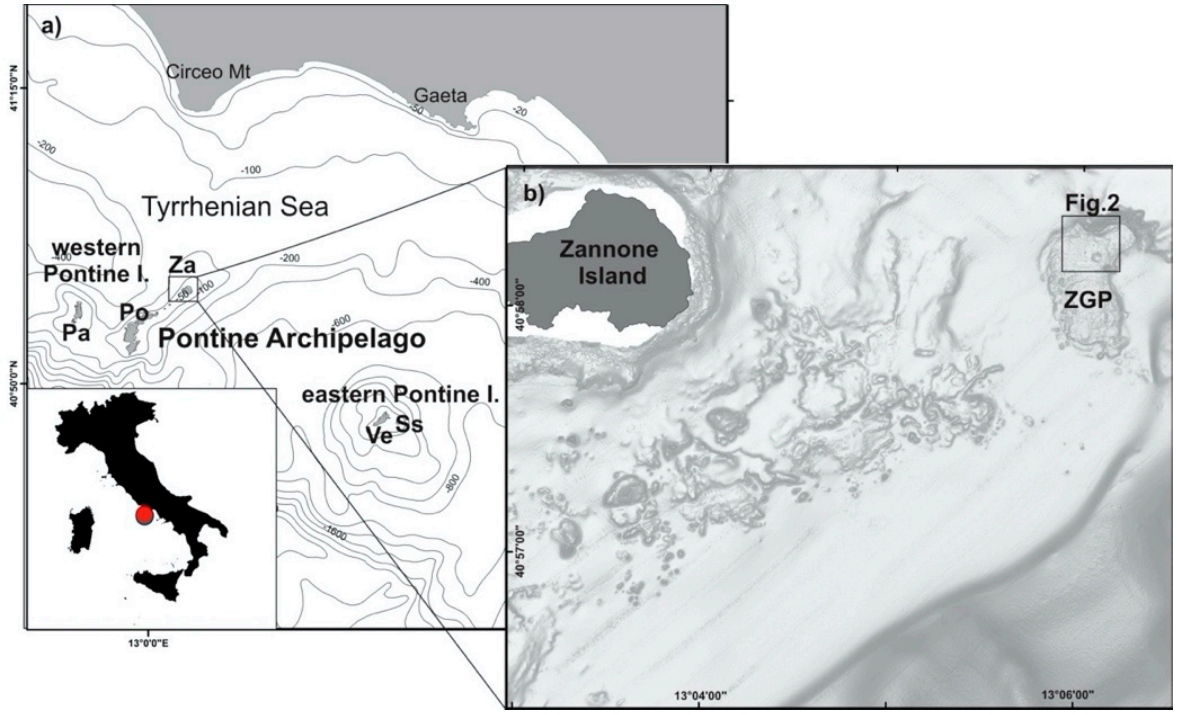


**Figure 1.** (**a**) Location of the Pontine Archipelago (Tyrrhenian Sea). Pa: Palmarola; Po: Ponza; Za: Zannone; Ve: Ventotene; Ss: Santo Stefano. (**b**) Shaded relief of the seafloor surrounding the Zannone Island, with the location of the Zannone Giant Pockmark (ZGP) where the seafloor samples were recovered. In the top right of Figure 1b, the rectangle identifies the area shown in Figure 2. Modified after Di Bella et al. [15].

The main depression of the Zannone hydrothermal field is the Zannone Giant Pockmark (ZGP), located about 3 km from the eastern coast of Zannone Island, between −110 m and −150 m (Figure 1). The ZGP is an elongated giant depression (900 m long, 15 m deep) characterized by a complex seabed morphology, likely related to the coalescence of crater-like features, possibly formed during

vigorous-explosive hydrothermal discharges [16]. Here, ongoing submarine hydrothermal activity is testified by fluid emissions and widespread bacterial mats (discharge sites are commonly marked by the occurrence of white bacterial mats) observed on ROV (Remote Operated Vehicle) surveys in many places, plumes observed on backscatter data of the water column, as well as by several fluid-venting morphologies at the seabed (small and large-scale pockmarks, mounds, cone-shaped structures, widespread authigenic crusts, and lithified pavements) [16,17]. The seafloor of the ZGP is covered by LGM (Last Glacial Maximum) [18] low-stand sandy deposits and by finer grained deposits of possible Holocene age. These deposits, along with Pleistocene sedimentary units, lie above a rocky substrate [16].

Several active fluid emissions have been identified at the ZGP seabed, characterized by discharge of clear thermal waters and bubbling gases. Maximum temperatures of 60–70 °C were measured at the seabed [19,20].

Geochemical analyses of the Zannone hydrothermal fluids indicate emission of $CO_2$-rich gases with a mantle-derived signature ($^3He/^4He$ of 3.72–3.75), with equilibrium temperatures ranging between 150 and 200 °C [17,20] and $H_2O$ pressures of ca. 5 bar [20]. The degassing suggests a significant contribution of mantle volatiles, possibly originated from residual magma batches similar to the Pleistocene trachytes cropping out in the SE sector of Ponza Island [17].

Although additional data (e.g., mineral and isotope compositions) would allow to better constrain the parameters that govern the alteration and mineralization processes, the results of this study provide first insights on alteration and mineralization processes related to hydrothermal activity at the ZGP, derived by minero-petrographic and geochemical features of seafloor samples collected close to active vents, and by geo-morphological information obtained by ROV videos and multibeam bathymetry.

## 2. Materials and Analytical Methods

High resolution multibeam bathymetry data were acquired using a Kongsberg EM 710 (100-70 kHz) echosounder (KONGSBERG MARITIME, Kongsberg, Norway) during the oceanographic cruise carried out onboard the research vessel Maria Grazia (National Research Council, Rome, Italy) in November 2009 (MAGIC_IGAG_1009). Bathymetric data were processed with CarisHips&Sips 8.1.7 software (TELEDYNE CARIS, Fredericton, NB, Canada). The ZGP seafloor high-resolution Digital Elevation Model (DEM) has been produced with a maximum cell-size of 0.5 m. Ground-truth data (i.e., ROV and grabs) were acquired during the oceanographic cruise "Bolle 2014" on board of the Urania research vessel (National Research Council, Rome, Italy). In detail, videos data were recovered using the ROV system "Pollux III (GEI)". The ROV was equipped with an underwater acoustic tracking positioning system (ultra-short baseline, USBL) providing detailed records of the seafloor tracks. The ROV was also equipped with a basket to recover crust samples (Table 1).

**Table 1.** List of grabs sampled within the Zannone Giant Pockmark (ZGP).

| Sample | Lat | Lon | Depth (m) | Analyzed Portion |
|---|---|---|---|---|
| ST2BNR1 | 40° 58′ 21′′ N | 13° 06′ 06′′ E | 135 | crust |
| ST2BNR2 | 40° 58′ 20′′ N | 13° 06′ 04′′ E | 130 | clasts |
| ST2BNR3 | 40° 58′ 21′′ N | 13° 06′ 06′′ E | 135 | crust |
| ST9BNR2 | 40° 58′ 20′′ N | 13° 06′ 04′′ E | 128 | clast |
| ROV6 | 40° 58′ 14′′ N | 13° 06′ 05′′ E | 128 | crust |

Note: coordinates system: Geographic WGS84.

Regarding the seafloor samples, a total of 4 grab samples (Table 1) have been selected as representative of the lithological variability of the hydrothermal deposits sampled within the ZGP. These deposits are represented by crusts and clasts; these latter were chosen in order to maintain the representativeness of the accumulation of clasts taken within the ZGP, in which macroscopic aspect and lithological variations are appreciable with the naked eye.

Each sample was extensively analyzed by optical microscopy to define the petrographic features, and by SEM-EDS to obtain the morphologies, microstructures and elemental composition. Back-scattered-electron images (BSE) and energy-dispersive X-ray (EDS) spectra were determined using a FEI-Quanta 400 scanning electron microscope equipped for microanalysis with an EDAX Genesis system at the SEM Laboratory of the Earth Science Department, Sapienza University of Rome (Italy). The identification of crystalline material was realized by Xray diffraction on sample powder, by a Brucker D500 diffractometer using CuK$\alpha$ radiation (n = 1.5418 Å), operating at 40 kV and 40 mA at a step size of 0.0250° at the Department of Earth Science, Sapienza University of Rome (Italy).

Chemical analyses including major and trace elements, were measured by ICP-AES and ICP-MS, respectively, at the Activation laboratories, Ancaster, Canada, following the "WRA + Trace 4 Lithoreaserch" protocol. Details on the chemical analysis methods can be found at: http://www.actlabs.com.

## 3. Results

### *3.1. Seafloor Morphology, ROV Visual Description and Macroscopic Description of Hydrothermal Deposits*

The hydrothermal deposits, represented by both gravel clasts and crusts, were recovered within the ZGP were ongoing hydrothermal activity was recently documented [17]. Gravel clasts were recovered by grabs within an elongated depression located in the northern sector of the ZGP. In details, the grab sample ST9BNR2 (A-B-C) was collected at −128 m, on the upper edge of the southern flank of the elongated depression adjacent to the escarpment bounding the northern sector of the ZGP (Figure 2). In this sector, ROV images show a seafloor mainly composed of sandy and gravelly sediment that harbors white bacterial mats (Figure 2). Gravel clasts are sub-rounded and have elongated-to subcircular shapes (Figure 2). They have a size ranging between 2 and 5 cm and are generally characterized by an outer rind, with thickness varying from few millimeters to about 1 cm, creamy-gray in color. Some of these clasts are characterized by the presence of an inner core with a white or black color.

The grab sample ST2BNR2 (A-B-C-D) is located at −130 m on the mid-part of the southern flank of the above-mentioned elongated depression (Figure 2). Grab ST2BNR2 recovered several clasts with rounded to sub-rounded shapes interspersed in a sandy sediment (Figure 2). These clasts have a size ranging between about 1 and 4 cm with a color varying from creamy and light to dark gray. Some of these are characterized by an outer rind creamy gray in color with thickness ranging between few millimeters to about 1 cm, as well as by the presence of an inner core light gray or dark gray in color.

Crusts deposits were recovered in two sites located in the northern (ST2BNR1) and north-eastern (ROV6) sectors of the ZGP (Figure 2). The ROV6 site is located in the north-eastern sector of the ZGP at −128 m, where a subcircular mega pockmark occurs at the seafloor (Figure 2). The sample was collected on the eastern flank of this mega pockmark where authigenic crusts with an arcuate shape are visible on ROV6 images of the seabed (Figure 2). The crusts have a metric size, rising from a sandy seafloor characterized by pockmarks and white patches of bacterial mats (Figure 2). Active emissions (bubbles/fluids) are present and fluid was pouring out from cracks and from holes. Moreover, areas colonized by brownish bacterial filaments are present. The collected crust fragment has a maximum thickness of about 5 cm and is formed by cemented sandy grains brownish in color with macroscopic evidence of microbial activity in form of organic mats (dark/gray layer) (Figure 2).

ST2BNR1 sample was collected in the northern sector of the ZGP at −135 m within the elongated depression adjacent to the northern escarpment bounding the ZGP (Figure 2). Here, ROV images of the seabed show the occurrence of sparse authigenic crusts, sparse clasts (centimetric surrounded clasts) and sandy sediment (Figure 2). The seafloor is pockmarked and active fluid emissions are present (Figure 2). The sediment recovered by grab sample is composed of sandy sediment, crusts and clasts. The ST2BNR1 sample is a sub-rounded crust formed by lithified sandy grains with presence of a yellow inner core formed by several nodules displaying mm-scale. This crust has a maximum

thickness of about 7 cm and was found interspersed in a warm sandy sediment characterized by a strong sulfur smell.

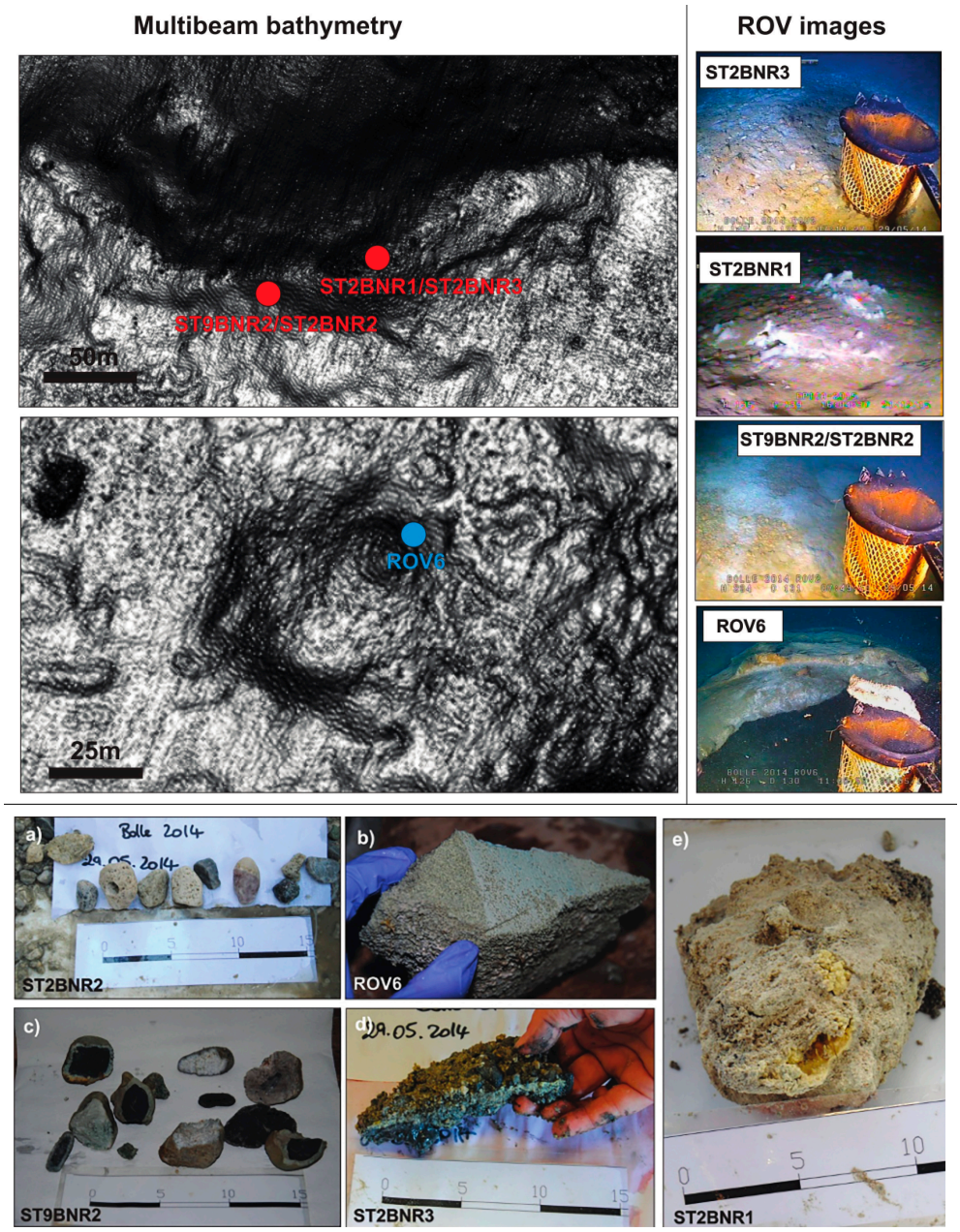


**Figure 2.** Multibeam bathymetry, ROV images of the sampled sites and images of the clasts (**a**,**c**) and crusts (**b**,**d**,**e**) analyzed in this study.

Finally, ST2BNR3 site is located at −135 m in the same site of sample ST2BNR1 (Figure 2). Grab sample includes sandy-gravelly sediment, authigenic crust fragments and black matter possibly resembling organic compounds (Figure 2). The ST2BNR3 crust appears composed of two layers. A top layer of black color formed by small cemented clasts and a homogeneous yellow bottom layer. This crust, with a thickness ranging from 1 and 2 cm, was found interspersed in a coarse sandy sediment with presence of several rounded and sub-rounded clasts.

### 3.2. Petrography

Four of the studied samples (ST2BNR2A, B, C, and D) are rhyolite lavas mostly displaying a preserved porphyritic primary texture, variably hydrothermally altered and silicified. Evidence of various degrees of hydrothermal alteration are represented by diffuse sericitization of primary K-feldspar phenocrysts, leaching of primary plagioclase phenocrysts, glass altered to crystalline hydrothermal quartz, mafic phenocrysts replaced by illitic clays, patches of clay and disseminated pyrite. The sole sample ST9BNR2B do not retains its primary texture and mineralogy being dominated by quartz and pyrite mineral association.

Based on dominant mineral assemblages and textural features different alteration facies can be defined among the studied samples, corresponding to alteration intensity [21–24]. In detail, ST2BNR2A is a moderately altered rhyolite, which mineral and textural assemblage likely correspond to a quartz-K-feldspar alteration facies. It displays a preserved porphyritic primary texture showing coarse K-feldspar in a siliceous, quartz-feldspathic groundmass. Primary K-feldspar phenocrysts are destroyed or replaced by sericitic alteration and/or hydrothermal phyllosilicates (illite-smectite, I-S), which also form patches in the microcrystalline groundmass. Rare precipitation of pyrite has been also observed (Figure 3).

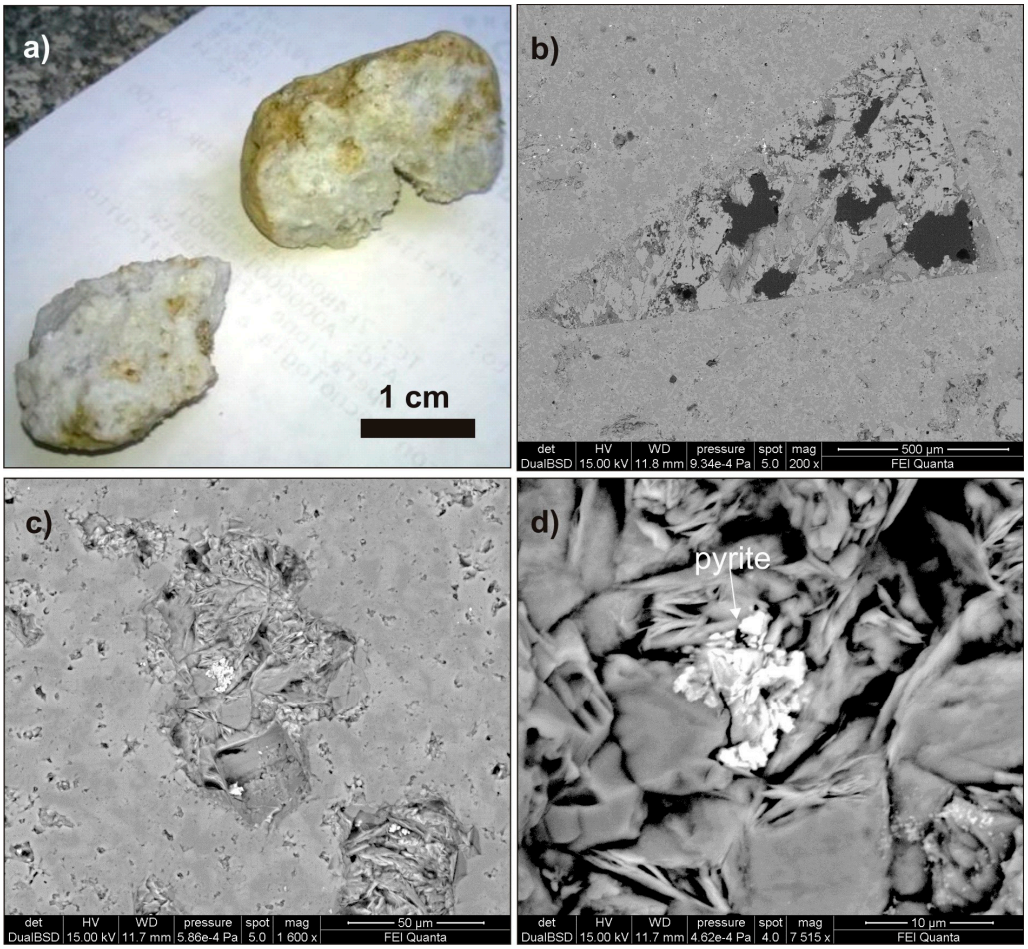


**Figure 3.** Hand specimen (**a**) and BSE images (**b**–**d**) of ST2BNR2A quartz-K-feldspar altered rhyolite. Partially sericitized K-feldspar (**b**), patches of phyllosilicates (**c**) including grains of pyrite (**d**) in the quartz-feldspathic matrix.

Sample ST2BNR2C is the least-altered quartz-K-feldspar porphyritic rhyolite likely corresponding to a feldspar-destructive alteration facies. It displays abundant K-feldspar and subordinate quartz

phenocrysts in a siliceous, quartz-feldspathic groundmass. Coarse phenocrysts of primary K-feldspar are well preserved in some cases, otherwise they are partially sericitized. Quartz phenocrysts have typical rounded shapes or smooth borders. Phyllosilicate (I-S) associated with hydrothermal alteration are relatively scarce in this sample forming rare patches or replacing occasional mafic phases (possibly pyroxene). Some accessories, such as rutile, zircon, and xenotime, are present throughout the sample (Figure 4; see Figure S1).

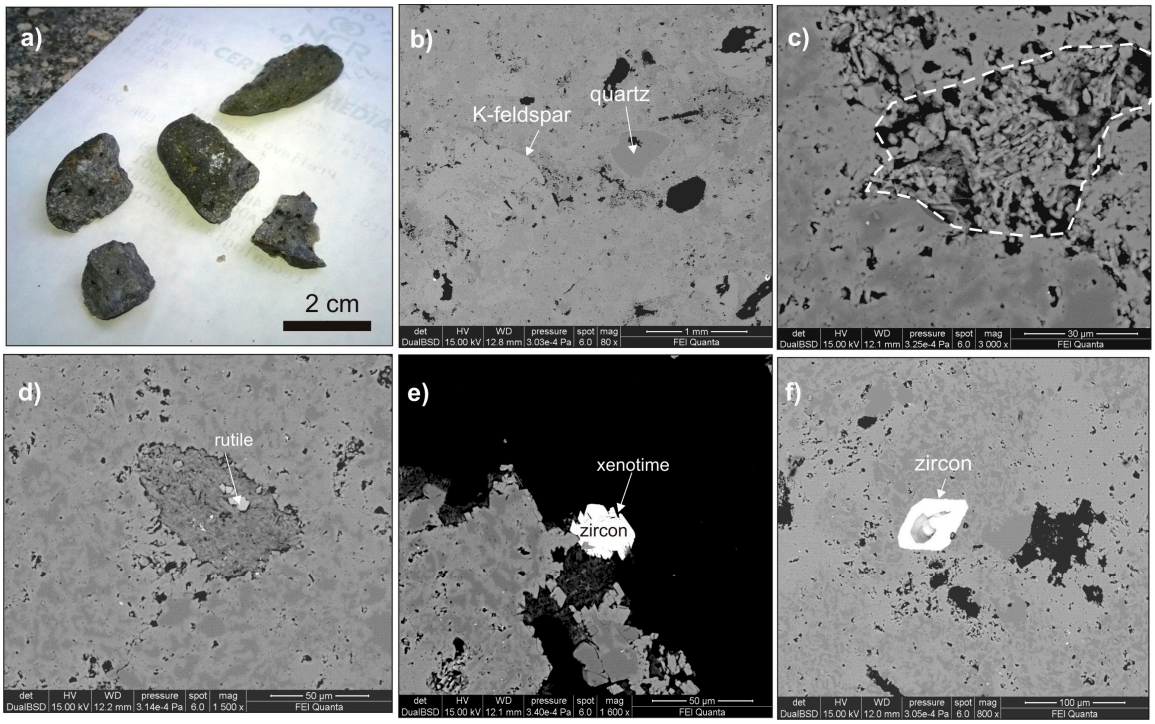


**Figure 4.** Hand specimen (**a**) and BSE images (**b**–**f**) of ST2BNR2C, feldspar-destructive altered rhyolite. Primary K-feldspar and quartz phenocrysts (**b**), patches of phyllosilicates (**c**), mafic crystal replaced by phyllosilicates and rutile (**d**), zircon crystal rimmed by xenotime (**e**) and zircon grain (**f**) in the quartz-K-feldspar matrix.

Sample ST2BNR2B is one of the most altered samples among the studied rhyolites. Its texture corresponds to a quartz-K-feldspar alteration facies with an incipient silicification. ST2BNR2B sample displays indeed a moderate porphyritic texture characterized by relatively scarce primary K-feldspar phenocrysts and hydrothermal phyllosilicate and a prevalence of authigenic quarz-K-feldspar association, with silicified zones, as well. (Figure 5a–f). ST2BNR2D is an altered rhyolite corresponding to a quartz-K-feldspar alteration facies showing a preserved porphyritic primary texture with K-feldspar phenocrysts partially sericitized or replaced by a phyllosilicate-dominated hydrothermal alteration that also forms patches in the microcrystalline quartz-K-feldspar groundmass (Figure 5g–n). It shares with the ST2BNR2B sample a peculiar occurrence of disseminated phases, such as pyrite, zircon, apatite, rutile, monazite, and Aluminum-Phosphate-Sulfate (APS) minerals (Figure S1).

Sample ST9BNR2C is a hydrothermally altered rhyolite, quartz-K-feldspar textured, similar to the previously described. However, it displays, in addition to partially to totally sericitized K-feldspar and quartz, several phenocrysts of authigenic albite, partial to completely replaced by hydrothermal phyllosilicates, and abundant biotite, which preserve the original habit but is destroyed to form illitic clay and aggregates of minute rutile grains at the expense of the biotite-derived titanium. Sample ST9BNR2C is also characterized by the presence of a whitish rind. This displays a quartz-K feldspar aggregate with minor broken biotite and sulfur (Table S1), while phyllosilicates and albite are lacking (Figure 6).

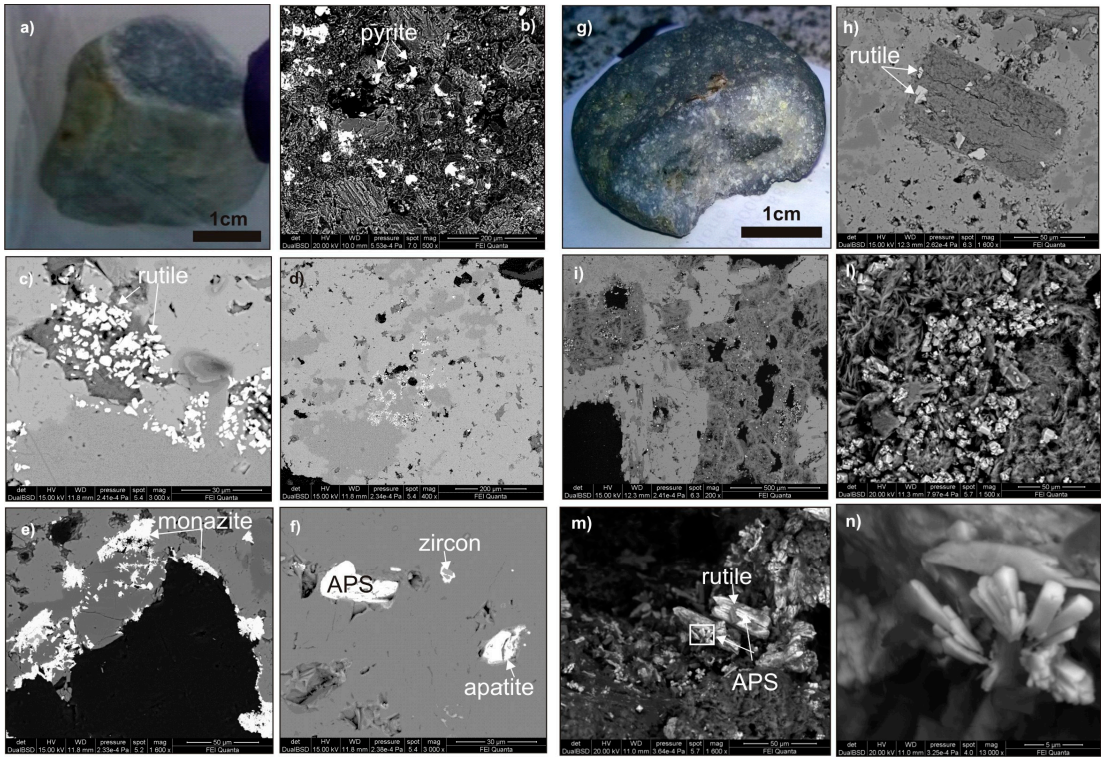


**Figure 5.** Hand specimen (**a**) and back-scattered-electron images (BSE) images (**b**–**f**) of ST2BNR2B quartz-K-feldspar altered rhyolite. Authigenic K-feldspar and quartz with disseminated pyrite (**b**–**d**); rutile crystals (**c**); cluster of monazite crystals associated with rutile grains (**e**); apatite, zircon, and Aluminum-Phosphate-Sulfate (APS) phases in authigenic K-feldspar (**f**). Hand specimen (**g**) and BSE images (**i**–**n**) of ST2BNR2D quartz-K-feldspar altered rhyolite. Mafic crystal replaced by phyllosilicates and rutile grains (**h**); partially destroyed primary K-feldspar with formation of hydrothermal phyllosilicates and hydrothermal rutile and pyrite (**i**,**l**); rutile crystals and APS phases (**m**); detail of APS crystals (**n**).

Finally, sample ST9BNR2B is the sole of the studied clasts representative of the intensely altered quartz-pyrite alteration facies. The inner, brown-gray portion of this sample displays an assemblage dominated by fine-grained quartz with some percentage (5–10%) of pyrite disseminated in grains and in small veins, illite phyllosilicate and minor calcite. (Figure 7; see Table S1). The white-outer layer of this sample, is about 5 mm tick and is made up by the sole microcrystalline quartz with very sparse pyrite and calcite (Table S1).

The three crusts sampled (ROV6, ST2BNR1, and ST2BNR3) are made up by sulfur. ROV6 and ST2BNR1 are sulfur-cemented sandy samples constituted by dominant quartz, feldspars, and plagioclase. The ROV6 crust includes grain of pyroxene and most feldspar crystals are anorthoclase (Na-rich K-feldspar; see Figure 8), while the ST2BNR1 samples include a small amount of barite (Table S1; see Figure 9).

ST2BNR3 sample is a sulfur crust which include clasts of altered rhyolite and quartz-pyrite and dark areas (Figure 10) made up by quartz, K-feldspar, hydrothermal phyllosilicates (illite, kaolinite), gypsum, rutile, and barite of sandy grain size.

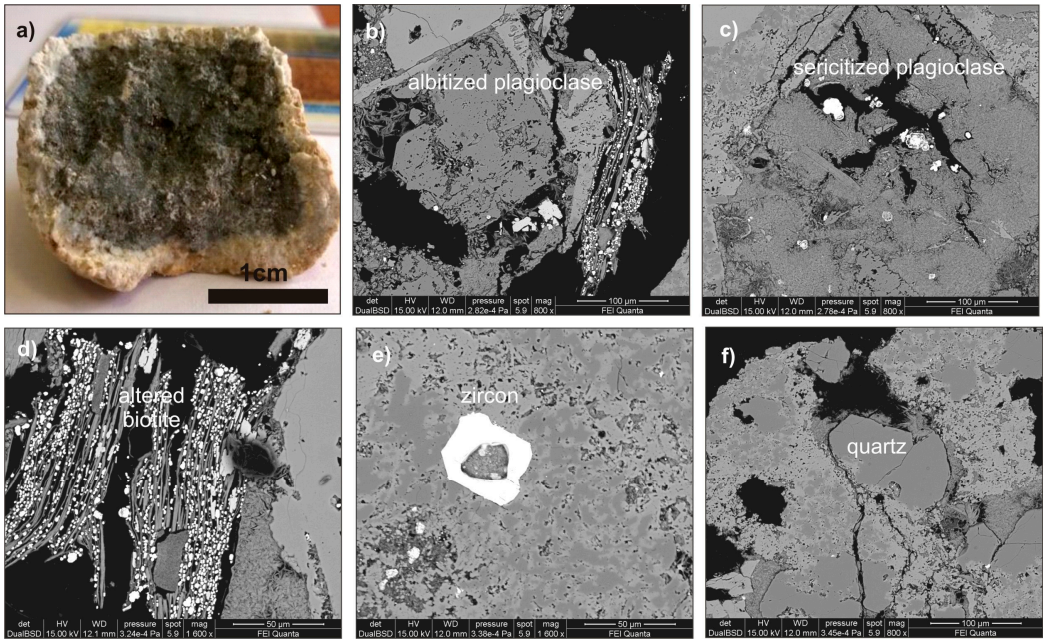


**Figure 6.** Hand specimen (**a**) and BSE images (**b**–**f**) of ST9BNR2C, quartz-K-feldspar altered rhyolite. Hydrothermal albite (**b**) partially replaced by phyllosilicates (**c**). Destroyed primary biotite with formation of hydrothermal phyllosilicates and rutile (**d**). Zircon in authigenic quartz-K-feldspar groundmass (**e**) with silicified zones (**f**).

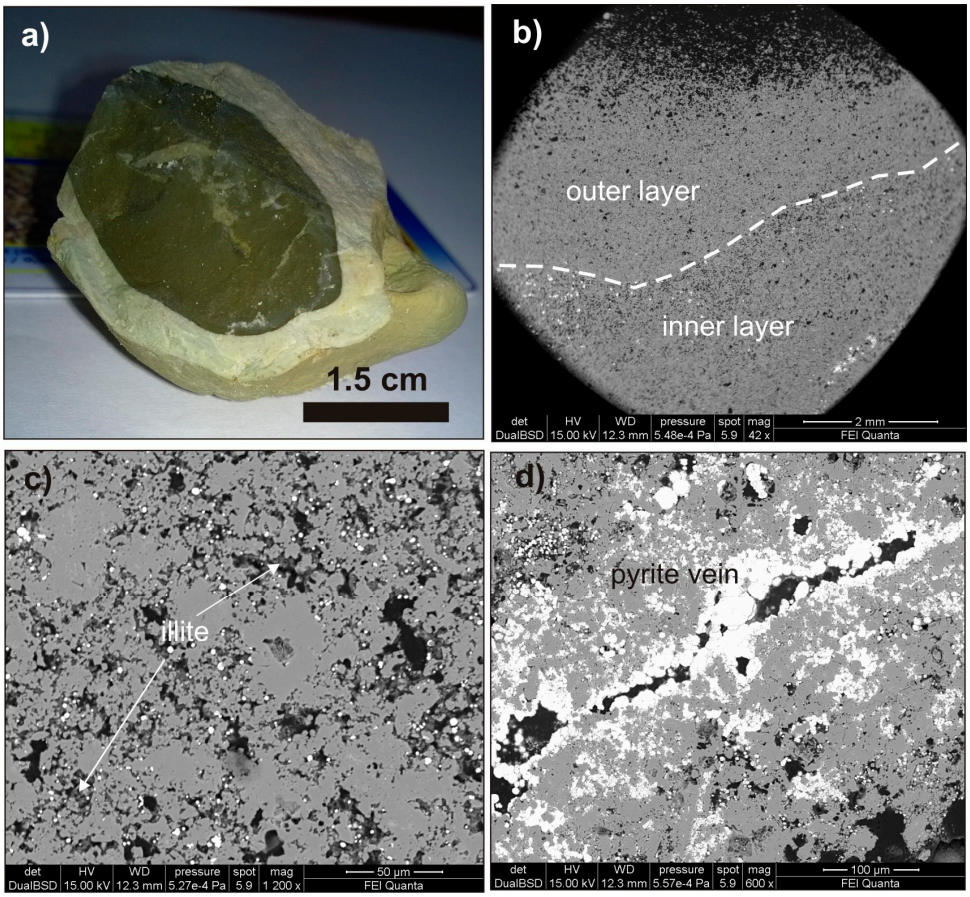


**Figure 7.** Hand specimen (**a**) and BSE images (**b**–**d**) of ST9BNR2B quartz-pyrite altered sample. Quartz-pyrite association with illitic patches (**c**) and pyrite veins (**d**).

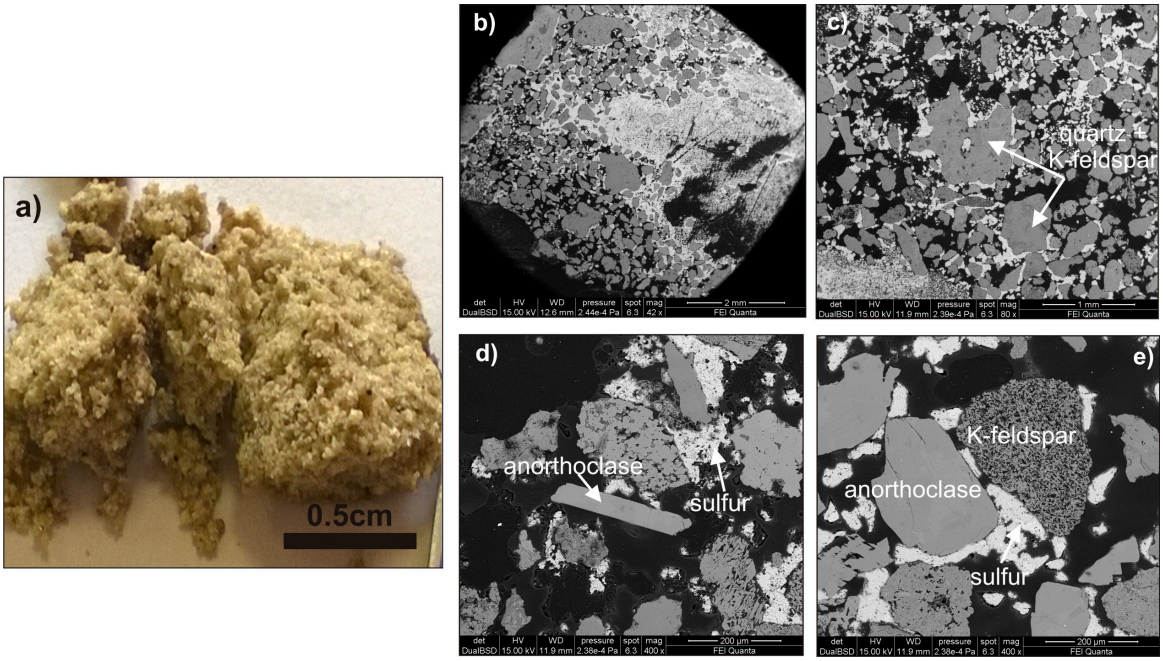


**Figure 8.** (**a**) macroscopic rock image of ROV6 sample. Sand is composed of quartz, K-feldspar, anorthoclase and plagioclase cemented by sulfur.; (**b**–**e**) SEM images showing the texture of minerals forming the sample.

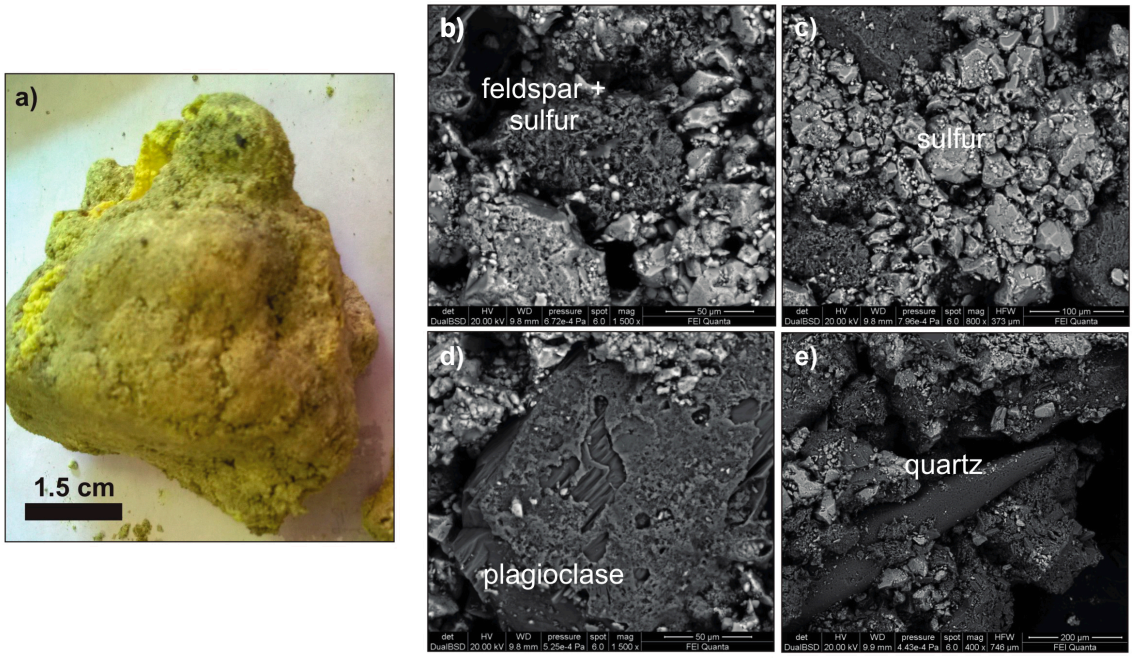


**Figure 9.** (**a**) macroscopic rock image of ST2BNR1 sample. Sand composed of quartz, K-feldspar, plagioclase, and barite cemented by sulfur. (**b**–**e**) SEM images showing the texture of minerals that form the sample.

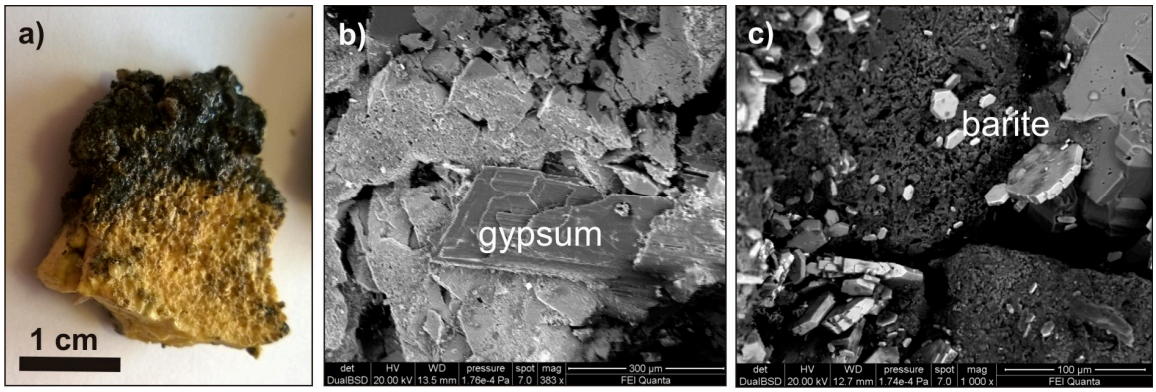


**Figure 10.** (**a**) macroscopic rock image of ST2BNR3 sulfur crust including (**b**) gypsum, and (**c**) barite.

### *3.3. Major and Trace Element Geochemistry of Rhyolite Clasts*

This section examines the major and trace element compositions of the ZGP rhyolite clasts which chemical analyses are presented in Table S2 (in Supplementary Materials).

#### 3.3.1. Major Element Geochemistry

ZGP clasts show limited compositional variations among them; some chemical differences are observed between the inner and outer part of a single clast. In order to evaluate the effect of hydrothermal alteration on these clasts, we used the Ishikawa alteration index (AI) and the chlorite–carbonate–pyrite index (CCPI) boxplot (Figure 11) that allows us to track the chemical and mineralogical changes associated with hydrothermal alteration and also to separate unaltered or weakly altered samples from those composition of which was affected by hydrothermal modification [23,25]. The alteration index ($AI = 100 \times [MgO + K_2O]/[MgO + K_2O + Na_2O + CaO]$ [25]) quantifies Ca and Na depletion and enrichment relative to Mg and K and then quantifies the intensity of sericite and chlorite alteration in the sample. The index varies from values of 20 about 60 for unaltered rocks and between 50 and 100 for hydrothermally altered rocks; an AI = 100 represents complete replacement of primary feldspar and glass by sericite and/or chlorite [23].

The chlorite-carbonate-pyrite index $CCPI = 100 \times [MgO + FeO]/[MgO + FeO + Na_2O + K_2O]$, instead, measures total alkali depletion relative to Mg and Fe enrichment associated with chlorite and pyrite formation and dolomite- and/or ankerite-rich carbonate precipitation.

Both inner and outer parts of all ZGP samples fall in the hydrothermal portion of the AI versus CCPI, and almost all arrange along the right-hand part of the box-plot due to their high AI (>88). The large range of CCPI (23–70) is related to variations in the proportions of sericite and pyrite, defining a trend toward the chlorite-pyrite alteration facies.

Figure 11 also shows the composition of subaerial products of Zannone Island [26], as well as unaltered and altered subaerial products of Ponza Island [27] and two samples (rhyolite s5 from Zannone and s13 rhyolite from Ponza submerged sector [28]) representative of compositions of fresh subalkaline Pliocene volcanism of the western Pontine Archipelago [13,14,28]. Zannone subaerial samples, partly overlapping the fields for the least altered rhyolites/dacites (AI = 33–57 and CCPI = 27–44) and of pyrite-rich alteration facies (AI = 95–97 and CCPI = 27–44), define different stages of hydrothermal alteration suffered by the Zannone subaerial products. Notably, the strongest altered subaerial samples (AI > 90) generally have higher CCPI values (49–91) than those of ZGP rhyolite clasts (CCPI = 23–60 for AI > 90), suggesting more intense alteration for the former subaerial rocks. Similar alteration trend is outlined by altered rhyolitic hyaloclastite samples from Ponza (Figure 11).

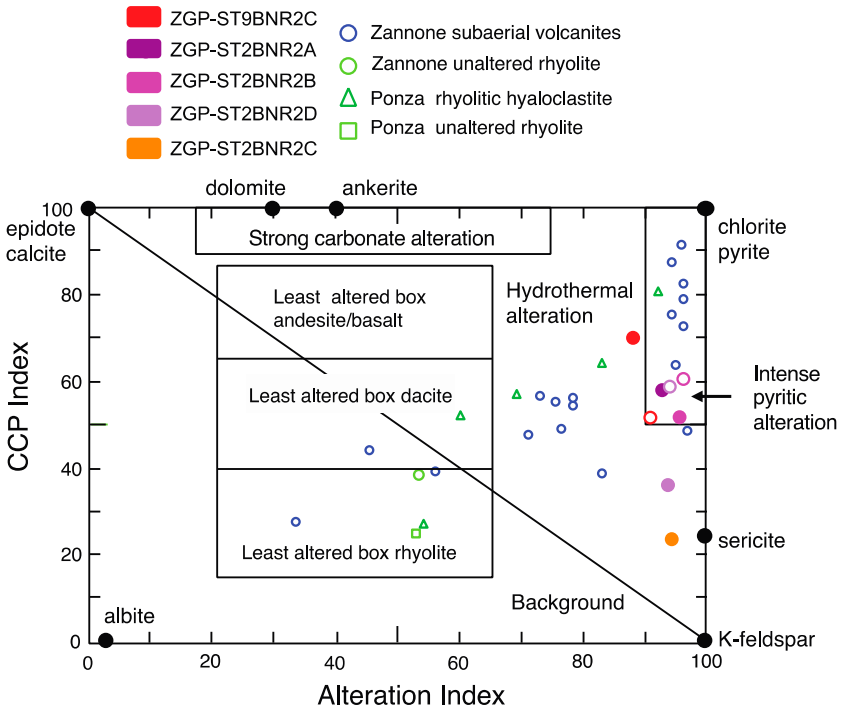


**Figure 11.** Alteration box plot with the Ishikawa alteration index (AI [25]) plotted against the chlorite–carbonate–pyrite index (CCPI; diagram after [23]). Symbols ZGP clasts: full—inner portion, empty—outer portion. Zannone subaerial volcanites are from Conte and Dolfi [26]; Zannone and Ponza unaltered rhyolites are samples s5 and s13 in Conte et al. [28]. Data representative of unaltered and weak to intense altered rhyolitic hyaloclastite from Ponza (argillitic, propylitic, silicic, and sericitic zones) are from Altaner et al. [27].

Compared to the fresh Zannone rocks and Pontine unaltered rhyolites, the main chemical character testifying alteration processes suffered by the ZGP clasts is their low $Na_2O$ contents (0.27–1.00 wt% ZGP-ST9BNR2C, with respect to 3.4–5.3 wt% in the fresh Zannone rhyolites; see Table S2 and Figure 12a). This coupled to the low CaO content (0.05–0.23 wt% with respect to 1.73–2.74 wt%) and the enrichment in $K_2O$ (8.27–10.96 wt% with respect to 5.07–5.72 wt%) and to a less extent of $SiO_2$, gives evidence of intense plagioclase phenocrysts destruction and formation of sericite (Figure 12b,c). Coherent with this indication are the values of the Spitz-Darling index ($Al_2O_3/Na_2O$ [29]) calculated for ZGP rhyolite clasts (Figure 12b). This index, reflecting the behavior of feldspars during hydrothermal alteration, increases from ~4.5 in unaltered Pontine rhyolites up to ~40 in the most $Na_2O$-depleted sample (ZGP-ST2BNR2B clast). The other mobile elements (Fe, Mg, and Mn) also display a depletion in almost all ZGP clasts, except sample ZGP-ST9BNR2C (inner portion; see Figure 12a), the $Fe_2O_3$ content of which is virtually the same of the Zannone unaltered rhyolite (2.12 and 2.24 wt%, respectively; see Table S2 in Supplementary Materials). Similar behavior of general depletion of MgO + $Fe_2O_3$ increasing the alteration intensity is observed in the Zannone subaerial samples, but, as in ZGP clasts, some intensely altered samples ($Na_2O$ < 0.5 wt%) are strongly depleted in MgO (up to the complete loss of this element) but enriched in $Fe_2O_3$ (up to 3.37 wt%; see Figure 12a).

It should be noted that some of ZGP clasts display a zonal alteration with their outer portion that is more depleted in $Na_2O$ contents and the other mobile major elements than the inner part (Figure 12 and Table S2).

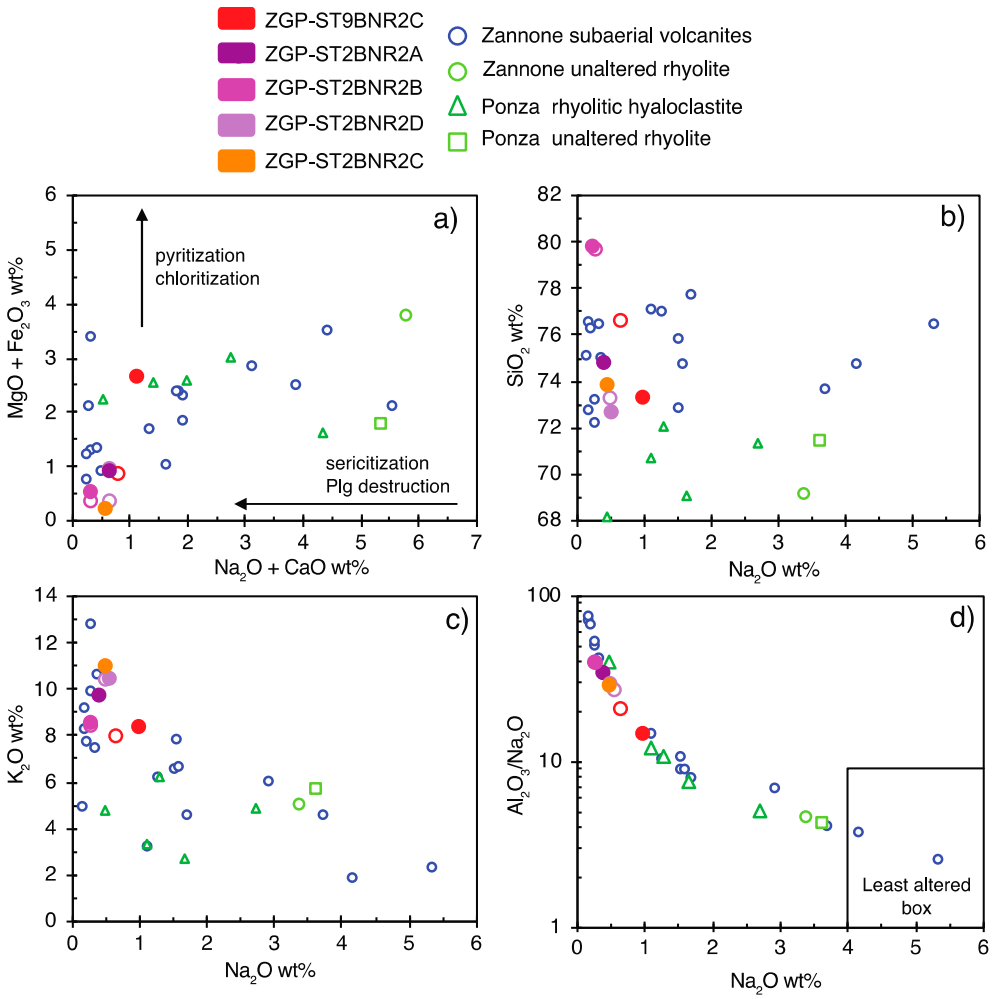


**Figure 12.** Mobile elements diagrams for ZGP clasts. (**a**–**c**) ZGP clasts show depletion in $Na_2O$, CaO, MgO, and FeO, suggesting that hydrothermal alteration was dominated principally by destruction of primary feldspar, sericitization, and pyritization processes that lead to Na, Ca, Mg, and Fe elements loss and gain of K and Si. (**d**) Spitz-Darling index [29] versus $Na_2O$ (diagram after [30]). Zannone subaerial volcanites are from Conte and Dolfi [26]; Zannone and Ponza unaltered rhyolites are samples s5 and s13 in Conte et al. [28]). Data representative of unaltered and weak to intense altered rhyolitic hyaloclastite from Ponza (argillitic, propylitic, silicic, and sericitic zones) are from Altaner et al. [27].

### 3.3.2. Trace Element Geochemistry

Due to the intense hydrothermal alteration of ZGP clasts, most of the major elements are not useful for their rock type classification. For these reasons, we used discrimination diagram for rock classification of Reference [31] based on the ratio of immobile elements (Nb/Y vs. $Zr/TiO_2$; see Figure 13a). All ZGP samples fall into the fields of subalkaline rhyolite-rhyodacite rocks with calcalkaline affinity (Figure 13b) as expected for the Pliocene Pontine volcanics. The REE (Rare Earth Elements) patterns normalized to chondrite CI [32] of ZGP clasts are almost identical to those of Zannone and Ponza unaltered rhyolites (Figure 13c), confirming that they are both good representative samples of background rocks for ZGP clasts. Of note is the depletion of Zr and REE which mainly concerns the ST2BNR2B sample, one of the most intensely altered quart-K-feldspar rhyolites (Figure 13b,c).

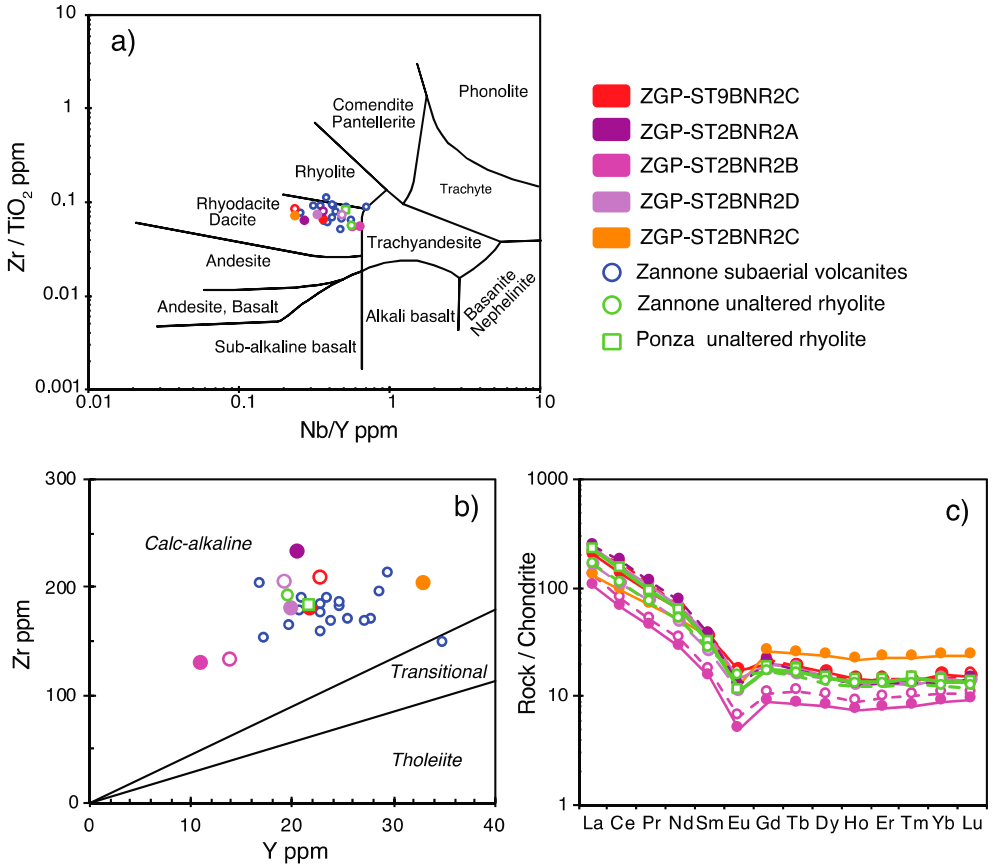


**Figure 13.** (**a**) Nb/Y vs, $Zr/TiO_2$ discrimination diagram for rock classification from [31]. (**b**) Zr-Y diagram for discriminating magma affinity from [33]. (**c**) Rare earth element (REE) patterns normalized to chondrite C1 [32] of the ZGP clasts. Zannone subaerial volcanites are from Conte and Dolfi [26]. Data of unaltered Zannone and Ponza volcanics are from Conte et al. [28]. Symbols ZGP clasts: full—inner portion, empty—outer portion.

Concentrations of Pb, Zn, As, Mo Ba, Rb, and Sr, were plotted against $Na_2O$, because Na depletion is an indicator of increased alteration intensity (Figure 14). As a rule, there is overlap and no clear correlation between alteration intensity and base metal concentrations.

The Pb and Zn show a slightly depletion or similar contents than those in unaltered samples except for ZGP-ST2BNR2B samples whose abundance in these elements is greater three /four times. Notably, concerning the most altered subaerial Zannone volcanics ($Na_2O$ < 1 wt%) for Pb and Zn these rocks show a contrasting behavior namely, an increase up to one order of magnitude in Pb associated with a significant depletion in Zn (down to 3 ppm; Figure 14a,b). Arsenic and Mo display a large variation with maximum values more than 10–100 times higher than in unaltered rhyolites (Figure 14c,d). A wide increase of concentrations is observed also for Tl and Sb which are positively correlated (Figure 14e).

Barium and Rb concentrations are strongly controlled by mineralogy of alteration (i.e., abundance of muscovite, K feldspar, or barite for Ba). Among ZGP clasts, Ba concentration increases up to ~1100 ppm in the ZGP-ST2BNR2B and ZGP-ST2BNR2C samples (Figure 15a), which record mineral associations dominated by K-feldspar and quartz with minor sericite, and accessory phases, such as apatite, monazite, and APS minerals likely related with mineralization processes (see Section 3.2). No clear Ba loss or gain is observed instead of the subaerial Zannone volcanics linked to hydrothermal alteration extent. Concerning Rb, its concentration in the ZGP clasts does not change significantly with respect to Rb contents of the unaltered samples as it is observed for the most altered samples ($Na_2O$ < 1 wt%) of Zannone which show an increasing trend (Figure 15b). The Sr is a good indicator of

feldspar-destructive alteration and generally decreases as the $Na_2O$ content decrease. Sr concentration of ZGP clasts of grab sample ST2BRN2 are clustered between 121 and 161 ppm, close to the Sr abundance of the Ponza unaltered sample (188 ppm) but clearly lower than the Ponza unaltered sample (270 ppm). Differently, Sr concentrations of the clast representing grab sample ST9BRN2 is less than 100 ppm (i.e., 83 and 65 ppm for inner and outer portions, respectively). Sr-ZGP abundances overlap the range of the intensely altered samples ($Na_2O$ < 1 wt%) of Zannone subaerial rocks (41–162 ppm) as shown in Figure 15c. The variable importance of the hydrothermal alteration processes linked to the formation of sericite and/or K-feldspar, replacing primary plagioclase, is evidenced by the variation of Ba/Sr ratio, which although shows a rough negative correlation with $Na_2O$ variation (Figure 15d).

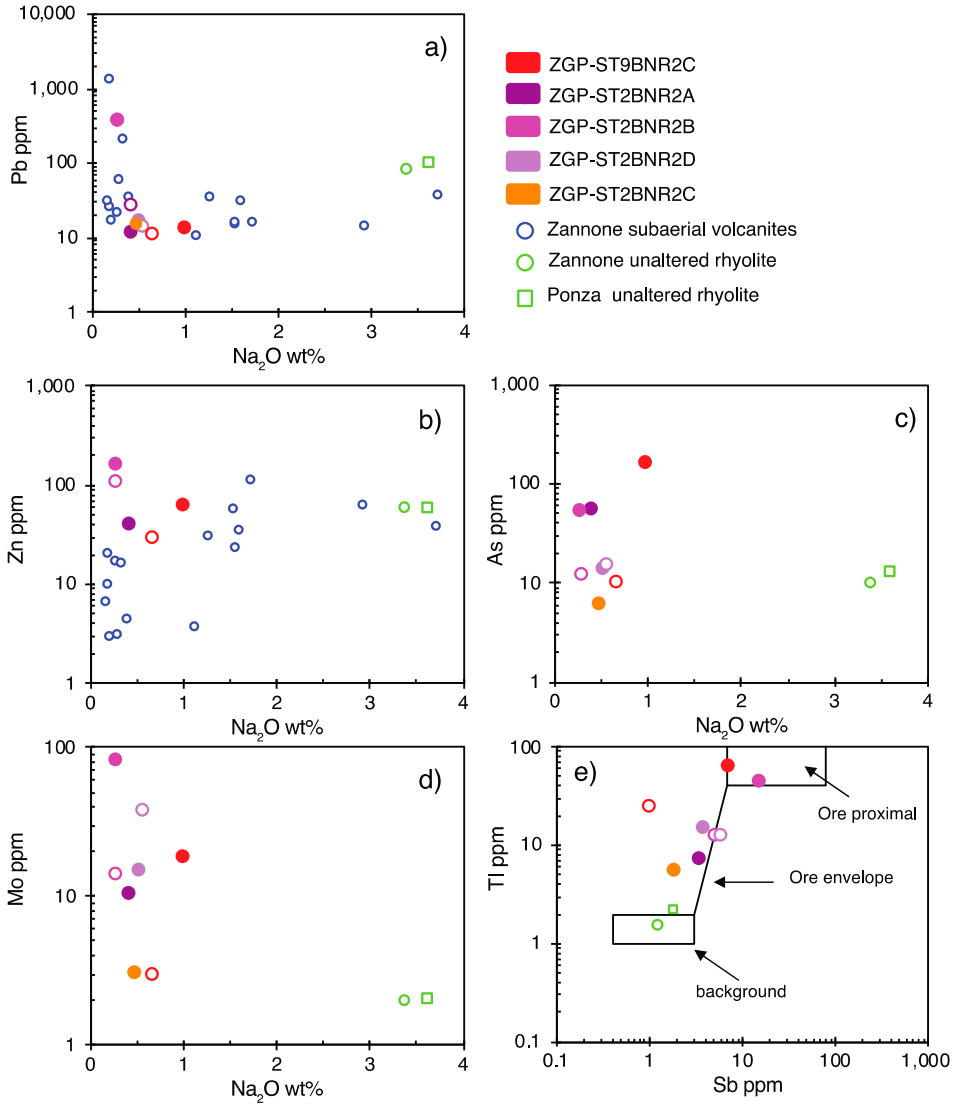


**Figure 14.** (**a**–**d**) Correlation plots of $Na_2O$ against selected base metal elements and As. (**e**) Relationship between Sb and Tl diagram for differently hydrothermal altered ZGP rhyolite clasts. The fields are from Large et al. [22]. Here and in Figure 15, Zannone subaerial volcanites are from Conte and Dolfi [26]. Data of unaltered Zannone and Ponza volcanics are from Conte et al. [28]. Symbols of ZGP clasts: full—inner portion, empty—outer portion.

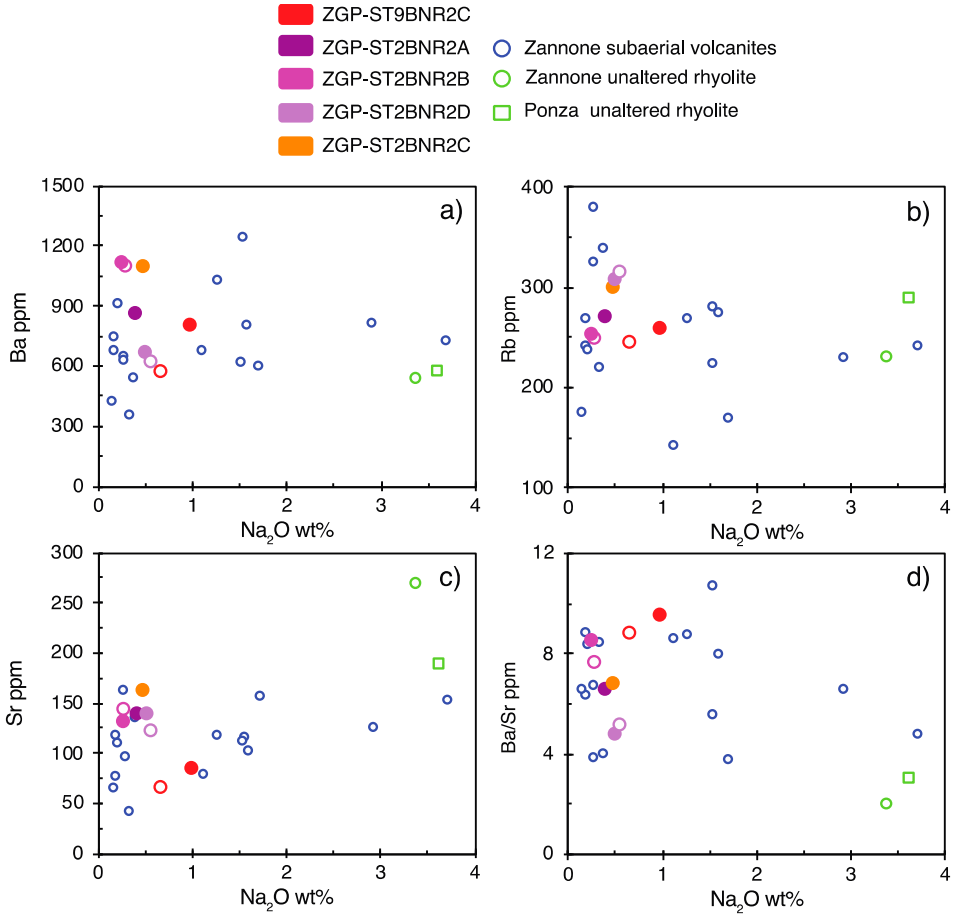


**Figure 15.** Correlation plots of (**a**) Ba, (**b**) Rb and (**c**) Sr trace elements versus $Na_2O$ concentration; (**d**) shows the variation of Ba/Sr ratio as function of $Na_2O$ depletion of altered ZGP rhyolite clasts. Zannone subaerial volcanites, unaltered Zannone and Ponza volcanics are as in Figure 14. Symbols of ZGP clasts: full—inner portion, empty—outer portion.

## 4. Discussion

### *4.1. Relationships Between ZGP-Rhyolite Clasts and Rhyolites of Western Pontine Islands*

The minero-petrographic observations and geochemical features of the studied clasts suggest that most of them are fragments of rhyolite lavas, similar to the Pliocene rhyolites of the western Pontine Islands (e.g., Reference [14]). Submarine outcrops of these lava types have been frequently recognized between Zannone and Ponza Islands, and in the southwestern submerged sector of Palmarola Island [28]. Optical microcopy revealed that the primary porphyritic texture (porphyritic index, P.I. ≥ 20 vol%) of ZGP rhyolite clasts are not completely obliterated by hydrothermal alteration. All rhyolite clasts contain the same primary minerals including K-feldspar as dominant phenocrysts joined by plagioclase + biotite ± quartz mineral assemblage. Moreover, although plagioclase and biotite alteration is particularly prominent, the scarcity of evidences of these minerals (relicts or authigenic mineral substitutes) suggests a low abundance in the original fresh rocks, except for sample ST9BNR2C in which a considerable amount of biotite remnants occur. This sample is also the only one in which the hydrothermal alteration produced authigenic albite, may be as a result of plagioclase albitization. The petrographic features of this clast suggest its initial significant modal abundance of biotite and plagioclase, a distinctive character of one of the main types of Pliocene rhyolite lavas outcropping in the western Pontine area [14,28]. These lavas are marked by porphyritic texture (porphyritic index, P.I. ≥ 15 vol%) with a phenocryst assemblage made up by plagioclase, biotite and minor K-feldspar. The other Kf-dominated ZGP rhyolites could instead represent the highly porphyritic variety of

subaphyric (P.I. ≤ 5 vol%) perlitic and/or fluidal textured, $SiO_2$-richest ($SiO_2$ > 71 wt%) rhyolites that, along with the rhyolitic hyaloclastite breccias, are the other typical Pliocene volcanic products of western Pontine islands. Indeed, as in the ZGP rhyolites, the dominant phenocryst phase of these subaphyric rocks is K-feldspar [14]. The narrow similarity of immobile trace element patterns between ZGP-rhyolites and fresh Pontine rhyolites (Figure 13c) suggests that before hydrothermal alteration on ZGP-rhyolites, their compositional uniformity was also for major elements. The textural differences between and fresh subaphyric Pontine rhyolites and ZGP-rhyolites can be ascribed to a pre-eruptive ponding stage of ZGP-rhyolite magma during which K-feldspars were able to form and grow.

### *4.2. Geochemical and Mineralogical Evidence of Hydrothermal Mineralization and Alteration Products at the ZGP*

Hydrothermal alteration of ZGP rhyolites mostly includes the destruction of primary feldspars, partially to fully replaced by sericite, silicification and formation of hydrothermal phyllosilicates (I-S), rutile aggregates (due to destruction of biotite), precipitation of disseminated pyrite (≤3 vol%) and complete replacement of primary matrix by authigenic quartz and K-feldspar. These textural and mineralogical features are similar to those described for the moderate to intense alteration zones, specifically feldspar-destructive, quartz-K-feldspar and quartz-pyrite alteration facies, associated with felsic volcanics hosting massive sulfide deposits that show characteristic zonal arrangements (distal to proximal) related to fluid flow and water/rock interaction processes (e.g., Reference [22,24,30]). The ST2BNR2C rhyolite is the least altered sample (scarce primary K-feldspar sericization and scarce hydrothermal clay mineral replacement of mafic pristine phenocrysts) and its CCPI value (23; see Figure 11) is similar to that of the weak sericite altered rocks usually found at the margins of a hydrothermal system (hanging wall and marginal footwall to ore deposit—Trend 1 in Reference [23]). The increase of CCPI at almost constant AI value of the other samples would imply an increase of sericite-chlorite ± pyrite alteration typical of the proximal alteration system to the ore deposit (Trend 2 in Reference [23]). However, petrographic observations and XRD analyses indicate that chlorite is always lacking, while quartz becomes increasingly abundant mineral of alteration assemblage in the other ZGP clasts. [23] have highlighted that the Alteration box-plot is unable to furnish any indications on the silicic alteration because both AI and CCPI do not include $SiO_2$ in their formula and then data of volcanic rocks affected by variably degree of silicic alteration most likely fall close to the sericite-chlorite join of the box-plot [23]. Thus, the shift of CCPI to higher values (up to ~ 70) of the ZGP rhyolite clasts appears to outline an alteration trend from distal to proximal ore deposit.

The quartz-K feldspar alteration facies recognized in most of ZGP rhyolite clasts, has been reported from several alteration zones associated with volcanic-hosted massive sulfide (VHMS) deposits. For instance, K feldspar has been observed in the outer parts of alteration systems associated with the Kuroko deposits in Japan [34,35], the Tasmania massive sulfide deposits (Australia, [22,24]), San Nicolás VHMS deposit (southern Zacatecas, Mexico [36]) or also associated with silicification and Au-rich mineralization (Que River deposit, Tasmania, Australia [37]). Moreover, the occurrence of K-feldspar in the alteration assemblage indicates a near-neutral pH of hydrothermal fluid (e.g., Reference [22]). Based on the observation of the quartz-K feldspar association on the alteration haloes associated with VHMS, Reference [24] argued that mixing of hydrothermal fluids with seawater at the margin of the hydrothermal system can cause simultaneous cooling and neutralization of the fluid, resulting in the formation of the quartz-K feldspar alteration facies. Thus, by analogy with these studies, it can be inferred that quartz-K-feldspar alteration of ZGP rhyolite clasts, formed most likely under low water/rock ratios at the outer zones of the hydrothermal system (e.g., Reference [24]) where relatively low temperature conditions occur. However, variations in the influx rate, temperature, composition, and pathways of the hydrothermal fluids may modify the position where the quartz-K feldspar alteration takes place.

Altaner et al. [27] studied the diffuse alteration zoning of hydrothermal altered rhyolitic hyaloclastite from Ponza Island produced by hydrothermal processes that were dated at 3.45–3.20 Ma.

The authors proposed four distinct alteration zones, namely, non-pervasive argillic, propylitic, silicic, and sericitic, differentiated by the authigenic mineralogy formed by interaction of hyaloclastite with hydrothermal fluids derived from sea water, at different water/rock ratios and different temperatures (30–90 °C for argillitic zone to 160–300 °C for the sericitic one). In particular, within the four alteration zones, the non-pervasive argillic one displays incomplete alteration of the hyaloclastite characterized by smectite and disordered opal-C, while the other three zones (propylitic, silicic, and sericitic zones) exhibit more complete alteration of the hyaloclastite. The propylitic zone is characterized by I-S minerals and opal-C plus authigenic K-feldspar while the silicic zone is characterized by I-S minerals, quartz, K-feldspar and occasional albite. In this zone, the matrix and clasts are completely altered, and pyrogenic plagioclase shows significant alteration. The sericitic zone consists primarily of I-S minerals, quartz, and minor K-feldspar and pyrite. Clay minerals completely replace pyrogenic feldspars and little evidence remains of the original hyaloclastite texture. Sulfate and sulfide minerals are relatively rare in these altered rocks.

When compared with the alteration zones described by Altaner et al. [27], mineralogical and chemical alteration changes observed in the ZGP rhyolite clasts approach to those of the silicic and sericitic zones, although some differences are observed between altered rocks of Ponza and ZGP. The main compositional difference concerns the opposite behavior of MgO content that with respect to the unaltered rhyolites Ponza rocks show a gain in samples of all alteration facies while in ZGP clasts MgO shows large depletion during alteration up to its almost complete loss in sample ST2BNR2C (0.07 wt%; see Table S2). Moreover, the ZGP rhyolite clasts display a ubiquitous $K_2O$ and $SiO_2$ gain, which, in the Ponza rocks group, is observed only in some samples of silicic alteration zone (Figure 12). According to Altaner et al. [27], which consider the MgO concentration in the altered rhyolites mostly deriving from seawater, the silicic alteration zone characterized by a low ratio between authigenic phyllosilicates and K-feldspar + quartz as in ST2BNR2C and ST2BNR2B samples, can be indicative of a relatively lower water/rock ratio (w/r) than that pertaining to the clay-richest, intensely altered sericitic zone (w/r ~6 and w/r ~9, respectively [27]). Actually, a low w/r ratio and a neutral to slightly basic pH of hydrothermal fluids can explain the K-feldspar + quartz association and also the relatively high Fe content of both the ST9BNR2C clast (Table S2 in Supplementary Materials) and some altered subaerial rocks of Zannone [24,27]. However, it should be noted that the w/r ratio cannot be considered the only parameter responsible for the concentration of MgO in the clay-richest, altered rhyolites. The extent of reaction and the replacement of rock with authigenic phyllosilicates, which affect the degree of Mg consumption in the clay-richest rhyolites, are regulated by other parameters such as the rock fabric and compositions and the variations in the ratio between hydrothermal magmatic fluids and seawater; the latter, in turn, determines the oxidation state and the pH of the interacting solutions. For instance, the attainment of reducing and relatively acidic conditions of the interacting fluids could account for the depletion of Fe concentration in the sericitic zone of altered Ponza rhyolites [27].

### *4.3. Geochemical Indicators of Proximity to a Possible VHMS Deposit*

In the framework of the mineralogical and geochemical variability of altered rhyolites, several mineral and geochemical features suggest occurrence of mineralizing processes. Sericite, illite, and smectite alteration minerals are consistent with the phase assemblages in modern submarine hydrothermal systems associated with massive sulfide mineralization at the sea floor [38–43]. Furthermore, quartz-pyrite alteration facies likely indicated by the ST9BNR2B sample, and that in some case exists as stratiform zones immediately below the massive sulfides (e.g., Reference [24,36]), is considered indicative of main fluid pathways during mineralizing hydrothermal activity (e.g., Reference [24]). This interpretation is supported by the high abundance of disseminated pyrite and pyrite veins, the substantially elevated concentrations of S, base metals (e.g., As, Mo, and Tl) and some trace elements (e.g., Ba or Rb).

Focusing on the inner part of ZGP rhyolite clasts, the concentrations of Tl, As, and Mo in these samples show and increase with respect to unaltered rhyolites ranging from 1(As, Mo, Sb) to 2 (Tl)

order of magnitude. The latter element in particular tends to increase in abundance with increasing of CCPI value of ZGP clasts (not shown) and with Sb concentration, showing a well correlation with the proximity to a possible ore deposit ([22,30]; see Figure 14). Ba concentration shows consistent changes in almost all samples and, in particular, in the Ba-rich samples ST2BNR2C and ST2BNR2B, which may indicate, respectively, a diffused sericitization of the K-feldspars for the least altered ST2BNR2C sample, or the vicinity to the massive sulfides for the intensely altered, silicified ST2BNR2B sample. This latter sample also displays a significant depletion of Zr and REE (Figure 13b,c), which mobility is linked to increasing intensity of hydrothermal alteration. Similar results have been also reported in ancient VHMS deposits (e.g., Reference [44]).

Therefore, both mineralogical and geochemical features suggest that the ZGP-altered rhyolites may represent altered clasts derived by deposits closely related to mineralized products formed in settings dominate by felsic volcanic rocks [39,45]. In these environments the upwelling of seawater-dominated, acidic fluids gave rise to a diffuse hydrothermal activity causing the destruction of primary feldspars, formation of hydrothermal sericite and clay minerals, and precipitation of pyrite. Then, the intense quartz-pyrite alteration was possibly directly associated with mineralization.

A further evidence for the possible proximity to mineralizing zones may be considered the presence of APS minerals, which were found in sparse amount in ST2BNR2B, ST2BNR2C, and ST2BNR2D altered rhyolite clasts, locally in assemblage with monazite. Monazite replacement by APS is quite common and such parental link is supported by geochemical evidences pertaining to REE and Th, which are close to those measured in the monazite residue, suggesting a monazite source for APS in some cases (Figure S1b,d). APS minerals are present in various environments and known to incorporate a great number of chemical elements in their lattice and to form complex solid-solution series controlled by the physic-chemical conditions of their formation (Eh, pH, activities of constituent cations, P and T [46]). In volcanic hydrothermal systems, their genetic setting indicates a magmatic volatile-rich hydrothermal environment, which stability temperature ranges between ~150 and 350 °C under highly acidic conditions. Interestingly, at Ontake volcano (Japan) [47], the APS minerals were found in ash deposits mainly composed of altered lithic fragments, brought to the surface by a magmatic-hydrothermal eruption, thus representing the trace of deep and higher-temperature alteration zones, in possible proximity to mineralizing systems. Here, the APS minerals have been related to highly acidic hydrothermal fluids existing beneath the volcanic summit, formed by condensation with magmatic and/or ground waters of magmatic volatiles exsolved from the magma chamber.

### *4.4. Implication for the ZGP Hydrothermal System*

The mineralogical and geochemical features of the collected samples, along with information on seabed morphology and lithologies of the sampled sites, point to the occurrence of ZGP of mineralization and alteration products formed by hydrothermal processes at the seabed. As shown in Section 4.1, the minero-petrographic and geochemical features of the clasts sampled from the seabed suggest that they formed as alteration products of rhyolite lavas. The finding of these altered rhyolites clasts suggests that a hydrothermal alteration halo of rhyolites lavas might be present beneath the ZGP seabed and its surroundings (Figure 16). Their occurrence at the seabed is intriguingly, as the rocky bedrock is buried by sedimentary deposits several tens of meter thick. Although, further work is needed to better constrain the emplacement at the seabed of these rhyolite clasts, a possible scenario encompassing explosive events determining brecciation of altered hosting rocks can be envisaged. These explosive events would be characterized by violent fluid discharge in focused venting (i.e., hydrothermal eruptions). The possible mechanism of emplacement is suggested by two main evidences: (1) the occurrence of the rhyolite clasts within the large crater-like depressions (i.e., the mega pockmark and the elongated depression observed on the multibeam bathymetry) that affect the Late Quaternary sedimentary deposits [16]. These depressions are known to be related to vigorous fluid escape from the seafloor, including sudden and violent eruptions [48] and at the ZGP have been related to vigorous hydrothermal eruptions [16]; and (2) the rounded shape of the hydrothermally altered rhyolite clasts.

In hydrothermal explosions, the rounded shape of clasts is determined by reworking (abrasion and milling) during their genesis (e.g., References [49,50] and references therein). Actually, it might have been originated also by other reworking processes, such as those related to sediment transport (e.g., fluvial transport in the subaerial environment); however, this process seems to be unlikely as the clasts show a well-preserved altered outer rim and occur at depth > 120 m.

Regarding to the mineralization products, the studied crust samples suggest that discharge activity in the ZGP results in the formation of authigenic crusts composed of native sulfur and native sulfur-cemented sandy sediment. Native sulfur is formed through many processes and conditions, which may include both abiotic and biological processes, and can be found in different geological environments, such as: hydrocarbon-bearing basins, volcanic and hydrothermal fields (e.g., the Kilauea volcano, the Lau basin caldera, the Manus basin), and several submarine arc volcanoes (e.g., Kermadec Arc, the Palinuro and Panarea volcanos; see [5,51] and references therein).

At the ZGP both multibeam bathymetry and backscatter data indicate diffuse discharge and mineralization, along with more focused discharge from isolated vents [16]. Moreover, the lithified crusts form different mineralization structures at the seafloor, such as: pavements, mounded structures, and arc-shaped and flange structures, as suggested by several seafloor observations [16]. As these structures are widespread at the ZGP seabed, where hard pavements possibly result from diffuse discharge favored by occurrence of thick porous sediment on the seafloor, it is likely that sulfur crusts might represent a significant hydrothermal mineralization product at the ZGP. Moreover, sulfur mineralization is possibly observed also in small chimneys located in the northern sector of the ZGP seabed [52].

At present, the origin of sulfur crusts at the ZGP cannot be fully constrained; however, available information suggests that they formed at the seafloor and/or in the shallow subsurface, as a result of sulfur precipitation from the rapid cooling of the gas phase of the ascending hydrothermal fluids [5,53]. In addition, mixing processes of mineralized hydrothermal fluids and seawater may form hydrothermal precipitates, such as barite [54,55]. Actually, as the native sulfur deposits of the ZGP are associated with white bacterial mats, it is also possible that biological processes (occurrence of sulfur bacteria) concurred to their formation (e.g., Reference [51]).

Native sulfur is commonly associated with sulfate sulfide, amorphous silica and hydrothermal alteration minerals (e.g., Reference [56,57]). Moreover, a similar association has been observed at the shallow water hydrothermal field off Panarea Island (Tyrrhenian Sea), where drilling showed that subcropping hydrothermal deposits consist primarily of anhydrite and gypsum with minor barite, marcasite, pyrite, sphalerite, alunite and kaolinite [3,4]. Although the study area does not represent the most typical environment for VHMS deposits (e.g., the Okinawa Trough [58,59]), several geological and tectonic features observed at ZGP are known to be favorable for formation of sulfide deposits at the seabed and in the subsurface [58,59]. They are: (1) the position of ZGP in the back-arc setting of the Tyrrhenian Sea, on a faulted structural high with extensive Plio-Pleistocene volcanism; (2) a well-developed hydrothermal system currently active; (3) the occurrence of host rhyolites; (4) the presence of sedimentary deposits; and (5) the discovery of the quartz-pyrite alteration facies and the APS minerals among the studied clasts that suggest the proximity to mineralizations (see Section 4.3). Since sulfide mineralization associated with felsic volcanic rocks [54] below the ZGP seabed cannot be excluded, a possible scheme of mineralization and alteration at the ZGP is proposed in Figure 16. However, further studies are needed to define the subseafloor hydrothermal structure and mineralization styles (e.g., massive, semi-massive, non-massive stockwork-like [60]) in this area.

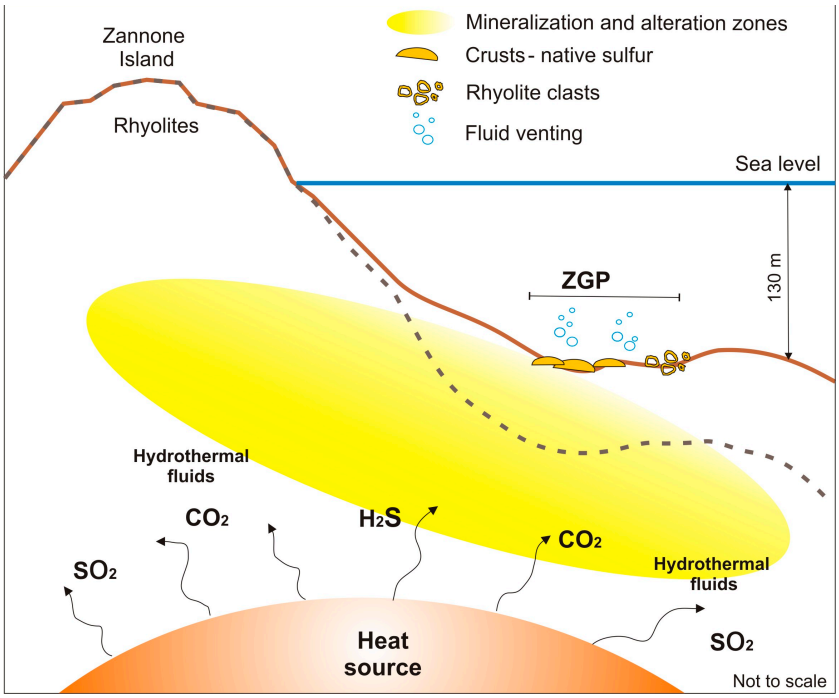


**Figure 16.** Sketch showing the possible occurrence of mineralization and hydrothermal alteration zones in the sub-surface of the ZGP. Dashed line indicates the probable top of the rhyolite substrata [16].

## 5. Conclusions

Hydrothermally altered and mineralized products have been identified at the Zannone Giant Pockmark (Zannone hydrothermal field, Tyrrhenian Sea) seabed with ongoing hydrothermal activity.

The geochemical and minero-petrographic analysis of seabed samples integrated by video observation and morphological characteristic of the sampled sites revealed that:

(1) among recovered samples, there are clasts moderately hydrothermally altered (quartz-K-feldspar alteration facies), due to destruction and sericitization of primary feldspars, and intensely hydrothermally altered ones showing silicified facies-quartz-pyrite alteration, pointing to different proximity to mineralizing/ore deposits;

(2) quartz-K-feldspar alteration of ZGP rhyolite clasts likely formed under low water/rock ratios at the outer zones of the hydrothermal system;

(3) the ZGP-rhyolites may represent altered clasts of felsic volcanic rocks similar to the Pliocene rhyolites outcropping on the western Pontine Archipelago;

(4) rhyolite clasts likely derive from hydrothermal eruptions determining explosive brecciation of altered hosting rocks beneath sedimentary deposits; and

(5) native sulfur crusts and native sulfur-cemented sediment likely form extensive mineralization products at the seabed, including different mineralization structures (e.g., pavements, as well as arc-shaped and flange structures).

All these evidences, along with the specific geological and tectonic setting of the western Pontine Archipelago, suggest that at the ZGP a sub-seafloor mineralization/sulfide formation associated with felsic volcanic rocks likely occurs.

**Supplementary Materials:** The following are available online at http://www.mdpi.com/2075-163X/10/7/581/s1, Figure S1: EDS spectra of APS minerals. Table S1: Mineral phases detected by the XRD analysis listed in order of decreasing abundance. Table S2: Chemical composition (major and trace elements) of ZGP clasts.

**Author Contributions:** A.M.C., L.D.B., M.I., E.M. collected the samples. A.M.C., L.D.B., M.I., C.P., E.M. prepared the samples and performed the analyses. M.I. and E.M. made the analyses of multibeam bathymetry and ROV images. A.M.C. and C.P. contributed the classification and geochemistry of the samples. M.I., C.P. contributed the editing of present versions of manuscript. All authors participated in the writing of the present versions of the manuscript. All authors have read and agreed to the published version of the manuscript.

**Acknowledgments:** The data used in this study were collected by CNR-IGAG (Rome, Italy) aboard of the Urania and Maria Grazia research vessels. We would like to thank captains, crews and participants of the oceanographic cruises. M. Albano and S. Stellino are gratefully acknowledged for their contribution in SEM-EDS and XRD analyses, respectively. Part of the research was performed in the framework of the Ritmare Project.

**Conflicts of Interest:** The authors declare no conflict of interest.

## References

1. De Ronde, C.E.J.; Hannington, M.D.; Stoffers, P.; Wright, I.C.; Ditchburn, R.G.; Reyes, A.G.; Baker, E.T.; Massoth, G.J.; Lupton, J.E.; Walker, S.L.; et al. Evolution of a submarine magmatic-hydrothermal system: Brothers volcano, southern Kermadec Arc, New Zealand. *Econ. Geol.* **2005**, *100*, 1097–1133. [CrossRef]
2. Hannington, M.D.; De Ronde, C.E.J.; Petersen, S. Sea-Floor Tectonics and Submarine Hydrothermal Systems. *Ecol. Geol. One Hundredth Anniv.* **2005**, 111–141. [CrossRef]
3. Peters, M.; Strauss, H.; Petersen, S.; Kummer, N.-A.; Thomazo, C. Hydrothermalism in the Tyrrhenian Sea: Inorganic and microbial sulfur cycling as revealed by geochemical and multiple sulfur isotope data. *Chem. Geol.* **2011**, *280*, 217–231. [CrossRef]
4. Monecke, T.; Monecke, J.; Reynolds, T.J. The Influence of $CO_2$ on the Solubility of Quartz in Single-Phase Hydrothermal Fluids: Implications for the Formation of Stockwork Veins in Porphyry Copper Deposits. *Econ. Geol.* **2019**, *114*, 1195–1206. [CrossRef]
5. Zeng, Z.; Liu, C.; Chen, C.A.; Yin, X.; Chen, D.; Wang, X.; Wang, X.; Zhang, G. Origin of a native sulfur chimney in the Kueishantao hydrothermal field, offshore northeast Taiwan. *Sci. China Ser. D Earth Sci.* **2007**, *50*, 1746–1753. [CrossRef]
6. Seewald, J.S.; Reeves, E.P.; Bach, W.; Saccocia, P.J.; Craddock, P.R.; Shanks, W.C.; Sylva, S.P.; Pichler, T.; Rosner, M.; Walsh, E. Submarine venting of magmatic volatiles in the Eastern Manus Basin, Papua New Guinea. *Geochim. Cosmochim. Acta* **2015**, *163*, 178–199. [CrossRef]
7. Hedenquist, J.W.; Lowenstern, J.B. The role of magmas in the formation of hydrothermal ore deposits. *Nature* **1994**, *370*, 519–527. [CrossRef]
8. De Ronde, C.E. Fluid chemistry and isotopic characteristics of seafloor hydrothermal systems and associated VMS deposits: Potential for magmatic contributions. In *Magmas, Fluids, and Ore Deposits*; Thompson, J.F.H., Ed.; Mineralogical Association of Canada Short Course Series: Ottawa, ON, USA, 1995; pp. 479–509.
9. Heinrich, C.A.; Halter, W.; Landtwing, M.R.; Pettke, T. The formation of economic porphyry copper (-gold) deposits: Constraints from microanalysis of fluid and melt inclusions. *Geol. Soc. Lond. Spec. Publ.* **2005**, *248*, 247–263. [CrossRef]
10. Yang, K.; Scott, S.D. Magmatic fluids as a source of metals in seafloor hydrothermal systems. *Wash. DC Am. Geophys. Union Geophys. Monogr. Ser.* **2006**, *166*, 163–184.
11. Yang, K.; Scott, S.D. Possible contribution of a metal-rich magmatic fluid to a sea-floor hydrothermal system. *Nature* **1996**, *383*, 420–423. [CrossRef]
12. Yang, K. Magmatic Degassing of Volatiles and Ore Metals into a Hydrothermal System on the Modern Sea Floor of the Eastern Manus Back-Arc Basin, Western Pacific. *Econ. Geol.* **2002**, *97*, 1079–1100. [CrossRef]
13. Cadoux, A.; Pinti, D.L.; Aznar, C.; Chiesa, S.; Gillot, P.Y. New chronological and geochemical constraints on the genesis and geological evolution of Ponza and Palmarola Volcanic Islands (Tyrrhenian Sea, Italy). *Lithos* **2005**, *81*, 121–151. [CrossRef]
14. Conte, A.M.; Dolfi, D. Petrological and geochemical characteristics of Plio-Pleistocene volcanics from Ponza Island (Tyrrhenian sea, Italy). *Mineral. Petrol.* **2002**, *74*, 75–94.
15. Di Bella, L.; Ingrassia, M.; Frezza, V.; Chiocci, F.L.; Martorelli, E. The response of benthic meiofauna to hydrothermal emissions in the Pontine Archipelago, Tyrrhenian Sea (central Mediterranean Basin). *J. Mar. Syst.* **2016**, *164*, 53–66. [CrossRef]

16. Ingrassia, M.; Martorelli, E.; Bosman, A.; Macelloni, L.; Sposato, A.; Chiocci, F.L. The Zannone Giant Pockmark: First evidence of a giant complex seeping structure in shallow-water, central Mediterranean Sea, Italy. *Mar. Geol.* **2015**, *363*, 38–51. [CrossRef]
17. Martorelli, E.; Italiano, F.; Ingrassia, M.; Macelloni, L.; Bosman, A.; Conte, A.M.; Beaubien, S.E.; Graziani, S.; Sposato, A.; Chiocci, F.L. Evidence of a shallow water submarine hydrothermal field off Zannone Island from morphological and geochemical characterization: Implications for Tyrrhenian Sea Quaternary volcanism. *J. Geophys. Res. Solid Earth* **2016**, *121*, 8396–8414. [CrossRef]
18. Peltier, W.R.; Fairbanks, R.G. Global glacial ice volume and Last Glacial Maximum duration from an extended Barbados sea level record. *Quat. Sci. Rev.* **2006**, *25*, 3322–3337. [CrossRef]
19. ZHF CRUISE. *Campagna Oceanografica ZHF 2017*; Responsabile Scientifico: Eleonora Martorelli; CNR-IGAG Roma: Roma, Italy, 2017.
20. Italiano, F.; Romano, D.; Caruso, C.; Longo, M.; Corbo, A.; Lazzaro, G. Magmatic Signature in Submarine Hydrothermal Fluids Vented Offshore Ventotene and Zannone Islands (Pontine Archipelago, Central Italy). *Geofluids* **2019**, *2019*, 1–15. [CrossRef]
21. Riverin, G.; Hodgson, C.J. Wall-rock alteration at the Millenbach Cu-Zn mine, Noranda, Quebec. *Econ. Geol.* **1980**, *75*, 424–444. [CrossRef]
22. Large, R.R.; Allen, R.L.; Blake, M.D.; Herrmann, W. Hydrothermal alteration and volatile element halos for the Rosebery K lens volcanic-hosted massive sulfide deposit, Western Tasmania. *Econ. Geol.* **2001**, *96*, 1055–1072. [CrossRef]
23. Large, R.R.; Gemmell, J.B.; Paulick, H.; Huston, D.L. The Alteration Box Plot: A Simple Approach toUnderstanding the Relationship between Alteration Mineralogy and Lithogeochemistry Associated with Volcanic-Hosted Massive Sulfide Deposits. *Econ. Geol.* **2001**, *96*, 957–971. [CrossRef]
24. Paulick, H. Alteration of Felsic Volcanics Hosting the Thalanga Massive Sulfide Deposit (Northern Queensland, Australia) and Geochemical Proximity Indicators to Ore. *Econ. Geol.* **2001**, *96*, 1175–1200. [CrossRef]
25. Ishikawa, Y.; Sawaguchi, T.; Iwaya, S.; Horiachi, M. Delineation of prospecting targets for Kuroko deposits based on modes of volcanism of underlying dacite and alteration halos. *Min. Geol.* **1976**, *26*, 105–117.
26. Conte, A.M.; Dolfi, D. *Note Illustrative e Carta Geologica in Scala 1:50.000 Delle Aree Marine del Foglio 413 Borgo Grappa*; ISPRA: Rome, Italy, 2018.
27. Altaner, S.P.; Ylagan, R.F.; Savin, S.M.; Aronson, J.L.; Belkin, H.E.; Pozzuoli, A. Geothermometry, geochronology, and mass transfer associated with hydrothermal alteration of a rhyolitic hyaloclastite from Ponza Island, Italy. *Geochim. Cosmochim. Acta* **2003**, *67*, 275–288. [CrossRef]
28. Conte, A.M.; Perinelli, C.; Bianchini, G.; Natali, C.; Martorelli, E.; Chiocci, F.L. New insights on the petrology of submarine volcanics from the Western Pontine Archipelago (Tyrrhenian Sea, Italy). *J. Volcanol. Geotherm. Res.* **2016**, *327*, 223–239. [CrossRef]
29. Spitz, G.; Darling, R. Major and minor element lithogeochemical anomalies surrounding the Louvem copper deposit, Val d'Or, Quebec. *Can. J. Earth Sci.* **1978**, *15*, 1161–1169. [CrossRef]
30. Piercey, S.J.; Squires, G.C.; Brace, T.D. Lithostratigraphic, hydrothermal, and tectonic setting of the Boundary volcanogenic massive sulfide deposit, Newfoundland appalachians, Canada: Formation by subseafloor replacement in a Cambrian rifted arc. *Econ. Geol.* **2014**, *109*, 661–687. [CrossRef]
31. Winchester, J.A.; Floyd, P.A. Geochemical discrimination of different magma series and their differentiation products using immobile elements. *Chem. Geol.* **1977**, *20*, 325–343. [CrossRef]
32. McDonough, W.F.; Sun, S.S. The composition of the Earth. *Chem. Geol.* **1995**, *120*, 223–253. [CrossRef]
33. Ross, P.-S.; Bédard, J.H. Magmatic affinity of modern and ancient subalkaline volcanic rocks determined from trace-element discriminant diagrams. *Can. J. Earth Sci.* **2009**, *46*, 823–839. [CrossRef]
34. Shirozo, H. Clay minerals in altered wall rocks of the Kuroko-type deposits. *Soc. Min. Geol. Jpn. Spec. Issue* **1974**, *6*, 303–311.
35. Shikazono, N.; Ogawa, Y.; Utada, M.; Ishiyama, D.; Mizuta, T.; Ishikawa, N.; Kubota, Y. Geochemical behavior of rare earth elements in hydrothermally altered rocks of the Kuroko mining area, Japan. *J. Geochem. Explor.* **2008**, *98*, 65–79. [CrossRef]
36. Vassallo, L.F.; Aranda-Gómez, J.J.; Solorio-munguía, J.G. Hydrothermal alteration of volcanic rocks hosting the Late Jurassic-Early Cretaceous San Nicolás VMS deposit, southern Zacatecas, Mexico. *Rev. Mex. Ciencias Geológicas* **2015**, *32*, 254–272.

37. McGoldrick, P.J.; Large, R.R. Geologic and geochemical controls on gold-rich stringer mineralization in the Que River Deposit, Tasmania. *Econ. Geol.* **1992**, *87*, 667–685. [CrossRef]
38. Alt, J.C.; Jiang, W.-T. Hydrothermally precipitated mixed-layer illite-smectite in recent massive sulfide deposits from the sea floor. *Geology* **1991**, *19*, 570. [CrossRef]
39. Binns, R.A.; Scott, S.D. Actively forming polymetallic sulfide de-posits associated with felsic volcanic rocks in the eastern Manus back-arc basin, Papua New Guinea. *Econ. Geol.* **1993**, *88*, 2226–2232. [CrossRef]
40. Goodfellow, W.D.; Grapes, K.; Cameron, B.; Franklin, J.M. Hydrothermal alteration associated with massive sulfide deposits, Middle Valley, northern Juan de Fuca Ridge. *Can. Mineral.* **1993**, *31*, 1025–1060.
41. Turner, R.J.W.; Ames, D.E.; Franklin, J.M.; Goodfellow, W.D.; Leitch, C.H.B.; HÖy, T. Character of active hydrothermal mounds and nearby altered hemipelagic sediments in the hydrothermal areas of Middle Valley, northern Juan de Fuca ridge: Data from shallow cores. *Can. Mineral.* **1993**, *31*, 973–995.
42. Ridley, W.I.; Perfit, M.R.; Josnasson, I.R.; Smith, M.F. Hydrothermal alteration in oceanic ridge volcanics: A detailed study at the Galapagos Fossil Hydrothermal Field. *Geochim. Cosmochim. Acta* **1994**, *58*, 2477–2494. [CrossRef]
43. Honnorez, J.J.; Alt, J.C.; Humphris, S.E. Vivisection and autopsy of active and fossil hydrothermal alterations of basalt beneath and within the TAG hydrothermal mound. In *Proceedings of the Ocean Drilling Program Scientific Results*; Herzig, P.M., Humphris, S.E., Miller, D.J., Zierenberg, R.A., Eds.; College Station, TX (Ocean Drilling Program), National Science Foundation: Alexandria, VA, USA, 1998; Volume 158, pp. 231–254.
44. Almodóvar, G.R.; Sáez, R.; Pons, J.M.; Maestre, A.; Toscano, M.; Pascual, E. Geology and genesis of the Aznalcóllar massive sulphide deposits, Iberian Pyrite Belt, Spain. *Miner. Depos.* **1997**, *33*, 111–136. [CrossRef]
45. Paulick, H.; McPhie, J. Facies architecture of the felsic lava-dominated host sequence to the Thalanga massive sulfide deposit, Lower Ordovician, northern Queensland. *Aust. J. Earth Sci.* **1999**, *46*, 391–405. [CrossRef]
46. Gaboreau, S.; Beaufort, D.; Vieillard, P.; Patrier, P.; Bruneton, P. Aluminum Phosphate-Sulfate minerals associated with Proterozoic unconformity-type Uranium deposits in the East Alligator River Uranium field, northern Territories, Australia. *Can. Mineral.* **2005**, *43*, 813–827. [CrossRef]
47. Imura, T.; Minami, Y.; Ohba, T.; Matsumoto, A.; Arribas, A.; Nakagawa, M. Hydrothermal Aluminum-Phosphate-Sulfates in Ash from the 2014 Hydrothermal Eruption at Ontake Volcano, Central Honshu, Japan. *Minerals* **2019**, *9*, 462. [CrossRef]
48. Hovland, M. The formation of pockmarks and their potential influence on offshore construction. *Q. J. Eng. Geol. Hydrogeol.* **1989**, *22*, 131–138. [CrossRef]
49. Chauvet, A. Structural control of ore deposits: The role of pre-existing structures on the formation of mineralised vein systems. *Minerals* **2019**, *9*, 56. [CrossRef]
50. Tămaș, C.; Milési, J. Hydrovolcanic Breccia Pipe Structures-General Features and Genetic Criteria. I. Phreatomagmatic Breccias. *Stud. Univ. Babes-Bolyai Geol.* **2002**, *47*, 127–147. [CrossRef]
51. Labrado, A.L.; Brunner, B.; Crémière, A.; Bernasconi, S.M.; Peckmann, J.; Giles, K.A. Thermochemical or microbial sulfate reduction: Determining the driver of native sulfur formation in the subsurface. In Proceedings of the AGU Fall Meeting, San Francisco, CA, USA, 9–13 December 2019; p. U11C–03.
52. Ingrassia, M.; Martorelli, E.; Italiano, F.; Macelloni, L.; Bosman, A.; Conte, A.M.; Di Bella, L.; Frezza, V.; Sposato, A.; Chiocci, F.L. Il sistema idrotermale al largo dell'Isola di Zannone (Mar Tirreno centrale): Nuovi risultati e prospettive. In Proceedings of the La Geologia Marina in Italia—Secondo Convegno dei Geologi Marini Italiani, CNR, Roma, Italy, 23–24 February 2017.
53. Yokoyama, Y.; Takahashi, Y.; Miyoshi, Y.; Ishibashi, J.I.; Kawagucci, S. Sediment–pore water system associated with native sulfur formation at jade hydrothermal field in Okinawa trough. In *Subseafloor Biosphere Linked to Hydrothermal Systems*; Ishibashi, J., Okino, K., Sunamura, M., Eds.; Springer: Tokyo, Japan, 2015; pp. 405–419.
54. Fouquet, Y.; Von Stackelberg, U.; Charlou, J.L.; Erzinger, J.; Herzig, P.M.; Muhe, R.; Wiedicke, M. Metallogenesis in back-arc environments: The Lau basin example. *Econ. Geol.* **1993**, *88*, 2154–2181. [CrossRef]
55. Conte, A.M.; Caramanna, G. Preliminary characterisation of a shallow water hydrothermal sulphide deposit recovered by scientific divers (Aeolian Islands, southern Tyrrhenian Sea). *Int. J. Soc. Underw.* **2010**, *29*, 109–115. [CrossRef]
56. Hannington, M.D.; Scott, S.D. Mineralogy and geochemistry of a hydrothermal silica-sulfide-sulfate spire in the caldera of Axial Seamount, Juan de Fuca Ridge. *Can. Mineral.* **1988**, *26*, 603–625.

57. Bach, W.; Roberts, S.; Vanko, D.A.; Binns, R.A.; Yeats, C.J.; Craddock, P.R.; Humphris, S.E. Controls of fluid chemistry and complexation on rare-earth element contents of anhydrite from the Pacmanus subseafloor hydrothermal system, Manus Basin, Papua New Guinea. *Miner. Depos.* **2003**, *38*, 916–935. [CrossRef]
58. Ishibashi, J.; Ikegami, F.; Tsuji, T.; Urabe, T. Hydrothermal Activity in the Okinawa Trough Back-Arc Basin: Geological Background and Hydrothermal Mineralization. In *Subseafloor Biosphere Linked to Hydrothermal Systems*; Ishibashi, J., Okino, K.M.S., Eds.; Springer: Tokyo, Japan, 2015; pp. 337–360.
59. Yeats, C.J.; Hollis, S.P.; Halfpenny, A.; Corona, J.-C.; LaFlamme, C.; Southam, G.; Fiorentini, M.; Herrington, R.J.; Spratt, J. Actively forming Kuroko-type volcanic-hosted massive sulfide (VHMS) mineralization at Iheya North, Okinawa Trough, Japan. *Ore Geol. Rev.* **2017**, *84*, 20–41. [CrossRef]
60. Eldridge, C.S.; Barton, P.B., Jr.; Ohmoto, H. Mineral textures and their bearing on the formation of Kuroko orebodies. In *Kuroko and Related Volcanogenic Massive Sulfide Deposits*; Economic Geology Monograph 5; Ohmoto, H., Skinner, B.J., Eds.; Economic Geology Publishing Company: New Heaven, CT, USA, 1983; pp. 241–281. ISBN 03610128.